Evidence for a lipofibroblast to collagen triple helix repeat containing 1^{positive} myofibroblast reversible switch during the development and resolution of lung fibrosis

Inaugural Dissertation
submitted to the
Faculty of Medicine in partial fulfillment of the requirements
for the PhD-Degree
of the Faculties of Veterinary Medicine and Medicine
of the Justus Liebig University Giessen

by
Lingampally, Arun Kumar Reddy
of
Kamalapuram, India

Giessen 2023

From the Department of Internal Medicine
and Cardio-Pulmonary Institute (CPI)
Director: Prof. Dr. Werner Seeger
Faculty of Medicine of the Justus Liebig University Giessen

First Supervisor: Prof. Dr. Saverio Bellusci

Co-supervisor: Prof. Dr. Bruno Crestani

Chair: Prof. Dr. Klaus-Dieter Schlüter

Second Supervisor / Vice-chair: Prof. Dr. Christoph Rummel

Date of Doctoral Defense

28.06.2023

Declaration

I declare that I have completed this dissertation single-handedly without the unauthorized help of a second party and only with the assistance acknowledged therein. I have appropriately acknowledged and referenced all text passages that are derived literally from or are based on the content of published or unpublished work of others, and all information that relates to verbal communications. I have abided by the principles of good scientific conduct laid down in the charter of the Justus Liebig University of Giessen in carrying out the investigations described in the dissertation.

_____

Arun Kumar Reddy Lingampally

Giessen, 2023

Dedicated to my family, my friends, and my mice ☺

Contents

List of Figures

List of Figures

Abbreviations and Acronyms

α-SMA	Alpha smooth muscle actin 2
Acta2	Actin alpha 2
Adrp	Adipose differentiation- related protein
Axin2	Axis inhibition protein 2
Apoe	Apolipoprotein E
aMYF	Activated myofibroblast
ASMC	Airway smooth muscle cells
AT1	Alveolar epithelial type 1
AT2	Alveolar epithelial type 2
Ampk	AMP-activated protein kinase
Aqp1	Aquaporin 1
Adh7	Alcohol dehydrogenase 7 (Class IV)
Bmp2	Bone morphogenetic protein 2
BSA	Bovine serum albumin
Col1a1	Collagen type I alpha 1 chain
Col3A1	Collagen type III alpha 1 chain
Col5a2	Collagen type V alpha 2 chain
Cdc-42	Cell division control protein 42 homolog
Cdh11	Cadherin 11
Ces1d	Carboxylesterase 1D
Cnn1	Calponin 1

Ccl11	C-C Motif chemokine ligand 11
CFE	Colony forming efficiency
Cthrc1	Collagen triple helix repeat containing 1
DAPI	4,6-diamidino-2-phenylindole
DLco	Diffusion capacity of the lung for carbon monoxide
ECM	Extracellular matrix
EMT	Epithelial to mesenchymal transition
Eln	Elastin
EpCAM	Epithelial cell adhesion molecule
FVC	Forced vital capacity
FDA	U.S. Food and Drug Administration
Fgf10	Fibroblast growth factor 10
Fgfr1b	Fibroblast growth factor receptor 1b
Fgfr2b	Fibroblast growth factor receptor 2b
FN1	Fibronectin 1
Fgf7	Fibroblast growth factor 7
Gli1	GLI family zinc finger 1
GFP	Green fluorescent protein
Hhip	Hedgehog interacting protein
IPF	Idiopathic Pulmonary Fibrosis
Inmt	Indolethylamine N-methyltransferase
Il6	Interleukin 6
LIF	Lipofibroblast

Limch1	LIM and calponin homology domains 1
Lgr5	Leucine rich repeat containing G protein-coupled receptor 5
Lgr6	Leucine rich repeat containing G protein-coupled receptor 6
Ltbp2	Latent transforming growth factor beta binding protein 2
Macf1	Microtubule actin crosslinking factor 1
Mmp3	Matrix metallopeptidase 3
Mapk	Mitogen-activated protein kinase
MANC	Mesenchymal alveolar niche cell
Neg	Negative
Npnt	Nephronectin
NFκb	Nuclear factor kappa-light-chain-enhancer of activated B cells
Plin2	Perilipin
Pdgfra	Platelet-derived growth factor receptor α
Pparγ	Peroxisome proliferator-activated receptor gamma
PBS	Phosphate buffered saline
PBST	Phosphate buffered saline with tween
Pos	Positive
PFA	Paraformaldehyde
Penk	Proenkephalin
Postn	Periostin
Pappa2	Pappalysin 2
Pthrp	Parathyroid hormone related protein
rMCs	Resident mesenchymal cells

rh	Recombinant human
RFP	Red fluorescent protein
Rbp4	Retinol binding protein 4
Robo2	Roundabout guidance receptor 2
SMC	Smooth muscle cells
scRNA-seq	Single-cell RNA sequencing
Sca1	Stem cells antigen 1
Sftpc	Surfactant protein C
Scube2	Signal peptide, CUB domain, and EGF like domain containing 2
Spp1	Secreted phosphoprotein 1
Sfrp1	Secreted frizzled related protein 1
Sparc	Secreted protein acidic and cysteine rich
Shh	Sonic hedgehog
Tgfβ	Transforming growth factor beta
Tcf21	Transcription factor 21
Tnfα	Tumor necrosis factor alpha
Tnc	Tenascin C
VSMC	Vascular smooth muscle cell
Vegf	Vascular endothelial growth factor A
Wnt5a	Wnt family member 5A

1. Introduction

1.1 Idiopathic pulmonary fibrosis

Idiopathic pulmonary fibrosis (IPF) is a chronic, fatal, and progressive lung disease with unknown etiology and cure. IPF is common in aged patients and is often diagnosed at the end stage of the disease. The median survival rate after the diagnosis is 2-3 years (Sgalla, Biffi, & Richeldi, 2016; Zhao, Kwan, Yip, Liu, & Liu, 2020).

The pathophysiology of the disease is poorly understood. However, it is widely accepted that the initiation of IPF starts with chronic inflammation and repetitive injury of the alveolar epithelium. Histologically, IPF is characterized by excessive extracellular matrix (ECM) deposition and tissue scarring resulting from an aberrant wound-healing process due to chronic injury in the alveolar compartment. The uncontrolled deposition of the ECM progressively leads to the disorientation of lung architecture, which results in the rigidity of the lung, and respiratory failure.

The pathological epithelial cells secrete pro-fibrotic and inflammatory mediators like cytokines, chemokines, matrix metalloproteins, and growth factors, which involve the chemotaxis and recruitment of activated myofibroblasts (aMYFs) in the fibrotic precursor region known as fibrotic foci (Mora, Rojas, Pardo, & Selman, 2017; Selman & Pardo, 2006).

Transforming growth factor-beta (TGFβ) during homeostasis is quiescent, bound to the ECM. However, during disease initiation and progression, TGFβ becomes activated in the ECM. Elevated TGFβ acts as a potent pro-fibrotic mediator, which drives the transition of resident lung fibroblasts to aMYFs (Fernandez & Eickelberg, 2012; Wipff, Rifkin, Meister, & Hinz, 2007; Zhao et al., 2020).

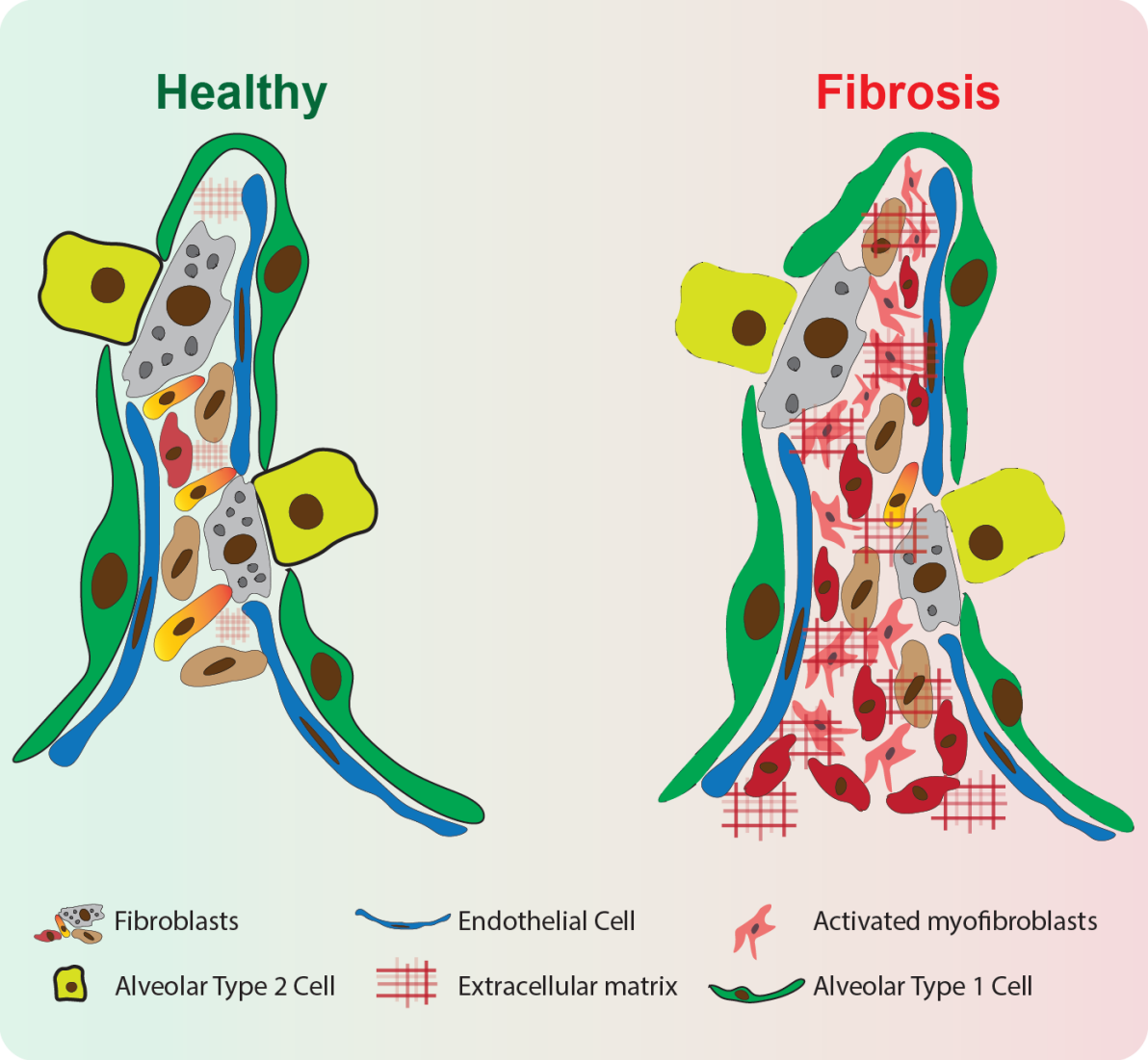

Figure 1: **Activated myofibroblasts in IPF.**

In healthy lung parenchyma epithelial and mesenchymal cells, crosstalk is essential for the maintenance of both alveolar structure and physiology. During fibrosis, interruption in the epithelial and mesenchymal crosstalk happens due to repetitive injury, which activates and drives massive recruitment of aMYFs. This recruited aMYFs deposit pathological ECM that eventually leads to the loss of alveolar structure and physiology.

1.2 Diagnosis and treatment of IPF

IPF is an age-associated disease and is often diagnosed in the elderly. Altered lung physiology due to loss of alveolar space by excessive tissue scarring leads to impaired gas exchange and lung failure. Symptoms include dyspnea, dry cough, bibasilar inspiratory crackles, and digital clubbing (Raghu et al., 2018).

High-resolution computed tomography, and in some cases, histology of surgical lung biopsy is used to visualize the presence of a reticular abnormality, honeycombing, traction bronchiectasis, and traction bronchiolectasis. Physiologically, patients manifest a decrease in the Diffusion capacity of the lung for carbon monoxide (DLco) and Forced Vital Capacity (FVC) (Plantier et al., 2018; Raghu et al., 2018; Sgalla et al., 2016).

Currently, only two drugs, pirfenidone, and nintedanib, have been approved by the FDA for treating IPF. Pirfenidone is an oral pyridine whose mechanism of action is not precisely known, though it shows anti-inflammatory and antioxidant properties. However, it is widely believed that the anti-fibrotic activity inhibits TGFβ signaling. On the other hand, nintedanib is a tyrosine kinase receptor inhibitor.

Despite this, these two medications are considered first-line therapy for IPF patients. Unfortunately, they only slow the progression but do not cure the disease; they often display tolerability issues and side effects (Y. M. Liu, Nepali, & Liou, 2017). Unfortunately, on long-term use, these two drugs show resistance and in due course, cause lung failure. Lung transplantation is the only intervention for end-stage IPF patients, and often the availability of a donor's lung is challenging.

1.3 Origin of aMYFs during IPF

Historically, modified fibroblasts/aMYFs were first observed in rat skin wound healing experiments. Histologically, these cells exhibited numerous folds with cytoplasm containing many stress fibers, identical to smooth muscle cells (SMC) fibers. These cells are proposed to be helping in wound contraction and healing. During wound healing, immune cells and fibroblasts get activated. This activated fibroblast at the site of injury deposits ECM and regulates matrix remodeling, which finally helps in wound closure. Following this complex process, the activated fibroblast undergoes apoptotic clearance

and reconstitutes normal tissue homeostasis (Gabbiani, Ryan, & Majne, 1971; Hung, 2020).

As aforementioned, IPF is a process characterized by repetitive injury to the alveolar epithelium, leading to the localization of aMYFs in the lung parenchyma as a response to the injury. However, these aMYFs resist apoptotic clearance, eventually leading to lung scarring. aMYFs acquire and express alpha-smooth muscle actin (α-SMA) and contain contractile filaments, as they are believed to be the key regulatory cells which secrete and deposit excessive ECM (El Agha, Kramann, et al., 2017; El Agha, Moiseenko, et al., 2017; Peyser et al., 2019; Phan, 2012) (Figure 1).

The cellular origin of aMYFs is still debated and controversial. Various studies anticipated and proposed that the aMYFs origin is not only a local but also systemic recruitment. Circulating fibrocytes expressing $CD45^{+}$ $COL1^{+}$ $CXCR4^{+}$, which are bone marrow-derived, are chemoattracted and recruited during fibrosis by tissue-derived chemokines (Phillips et al., 2004). Pericyte's contribution to aMYFs is still unclear; studies show that the Pericytes cells, such as FoxD1-lineage cells, contribute to aMYFs (Hung, 2020). In addition, $ABCG2^{positive(pos)}$ pericytes contribute to aMYFs (Marriott et al., 2014). In another study, only a minor contribution of NG2 lineage pericytes contributed to aMYFs (Rock et al., 2011). These studies suggest that pericytes are a heterogenous population that needs further characterization in the lung. Another source of aMYFs is alveolar epithelial type 2 (AT2) cells through a process of epithelial to mesenchymal transition (EMT) (Kim et al., 2006). This process is debatable as lineage tracing studies of AT2 cells in mice didn't contribute to newly formed myofibroblasts foci (Rock et al., 2011). Interestingly, current studies in human IPF lungs observed a new epithelial population of so-called aberrant basaloid lining the fibrotic foci, displaying both epithelial and mesenchymal signatures suggesting EMT (Adams et al., 2020; Habermann et al., 2020). Another potential and important source is resident mesenchymal cells (rMCs) in the lung. A recent study using $Col1a1^{GFP}$ mice showed the significance of rMCs and their contribution to aMYFs (Tsukui et al., 2020). In our studies using $Adrp^{CreERT2}$ (the lineage-labeled cells), which are lipofibroblasts (LIFs), differentiate into aMYFs during fibrosis (El Agha, Moiseenko, et al., 2017). Given all these cellular origins of aMYFs, it is rational to consider that aMYFs are

a heterogeneous population that has not been clearly understood and characterized until now.

1.4 Lipofibroblast in mice and human

Lung fibroblasts are quite diverse, and most fibroblast populations often overlap with their gene expression signature. Therefore, the diversity of the different types of fibroblasts in the lung is still unclear. However, recent studies attempted to distinguish these populations as peribronchial, adventitial, and alveolar fibroblasts (mainly consisting of LIFs) (Tsukui et al., 2020).

Historically, during the 1970s, two distinct types of interstitial cells were observed in embryonic rat lungs, namely, the non-lipid interstitial cell and the lipid interstitial cell (LIF) (O'Hare & Sheridan, 1970; Vaccaro & Brody, 1978). LIFs are lipid droplet-containing cells and are often identified by the expression of Perilipin (Plin2). During mouse lung development, the onset of LIFs was noticed at the end/late pseudoglandular stage.

Various genetic tracing studies in mice were employed to identify the origin and development of the LIFs. During lung development, LIFs originate from mesenchymal progenitors expressing fibroblast growth factor 10 (Fgf10). Fgf10, acting via both Fgfr1b and Fgfr2b, acts in an autocrine fashion on the mesenchymal progenitors to promote their differentiation towards the LIF lineage. Interestingly, during embryonic lung development, disruption of the Fgf10 signaling axis, even by ablating a single allele of *Fgf10*, or its receptor *Fgfr2b*, exhibited a significant decrease in LIFs formation at birth (Al Alam et al., 2015; El Agha et al., 2014). Postnatally, during homeostasis, Fgf10 helps in the maintenance of LIFs (Taghizadeh et al., 2021). These studies show that Fgf10 is a potent mitogen in regulating the development and conservation of LIFs in mouse lungs.

In another study using $Gli1^{CreERT2}$ mice, the lineage-labeled cells significantly contributed to LIFs at the time of birth (Moiseenko et al., 2017). Additionally, in a recent study using $Tcf21^{CreERT2}$ mice, the lineage-labeled cells contribute to the development of LIFs and help in the maintenance postnatally (J. Park et al., 2019). Furthermore, in the adult lung, LIFs also express Platelet-derived growth factor receptor α (Pdgfra) (Barkauskas et al., 2013).

As of today, no distinguishable genetic marker has been discovered, which is the main reason for the discrepancy in identifying the LIFs in the human lungs. LIFs were often identified by staining their characteristic lipid bodies, which is challenging to identify in the human lungs (Tahedl, Wirkes, Tschanz, Ochs, & Muhlfeld, 2014). In contrast, a recent study using advanced microscopy such as transmission electron microscopy, verified the presence of LIFs in the human lungs (Schipke et al., 2021).

In summary, despite multiple genetic origins of LIFs, only a fraction of the lineage-labeled cells contribute to LIFs pool, which shows the complexity of LIFs origin and development. In addition, recent advanced studies using scRNA-seq (Single-cell RNA sequencing) in humans and mice proposed that Limch1 and Apoe are notable markers for the LIFs (X. Liu et al., 2021; Travaglini et al., 2020).

1.5 LIF-AT2 interactions and AT2 stem cell niche

Anatomically, LIFs are located in close proximity to AT2 cells. They are characterized by a high level of lipid droplets and have been reported to provide AT2 cells with triglycerides, a fundamental building block of surfactant production (Figure2).

Our recent works suggest that Fgf10 signaling is crucial for the epithelial branching morphogenesis of the developing lung. Furthermore, Fgf10 arising initially from the LIF progenitors guides the differentiation of the alveolar epithelial progenitors during embryonic development (Jones et al., 2018; Jones et al., 2019; Jones et al., 2020). LIF-AT2 reciprocal interaction is also at play in the adult lung. Inactivation of *Fgfr2b* in the AT2s leads to their death. Hence suggesting that Fgfr2b ligands, which include Fgf10, are produced by the adjacent LIFs, and act on AT2 cells to maintain their survival in homeostatic conditions (Ahmadvand et al., 2021) (Figure17). Fgfr2 signaling in AT2 cells has also been shown to sustain AT2 identity during alveologenesis (Brownfield et al., 2022; Liberti et al., 2021).

Significant efforts have focused on the LIFs interacting with AT2s. The most commonly used is the alveolosphere model, which consists of co-culturing LIFs with AT2s in

matrigel. In this model, we can visualize the self-renewal of the AT2 stem cell as well as their differentiation towards AT1 cells (Barkauskas et al., 2013; McQualter et al., 2013).

A study using Pdgfra^{high} rMCs represented a niche for AT2 progenitor cells (Barkauskas et al., 2013). Another study proposed Lgr5 mesenchymal cells act as a niche for AT2 cells (Lee et al., 2017). Further refinement of the rMC population enabling the self-renewal and differentiation of AT2 progenitor cells led to the identification of mesenchymal alveolar niche cells (MANCs), positive for *Axin2*, *Pdgfra,* and *Fgf7* (Zepp et al., 2017).

In addition, our studies showed that a mesenchymal niche defined as CD45/CD31/EpCam-negative and Stem cells antigen-1 (Sca1)/Fgf10 positive, distinct from the MANCs, was also instrumental in the maintenance of AT2s. rMC Sca1^{pos} Fgf10^{pos} cells belong to the alveolar fibroblast lineage and have been proposed to be LIFs (Taghizadeh et al., 2021).

Given the background, LIF-AT2 reciprocal interactions are crucial during lung development and maintenance and homeostasis of the adult lung. Loss of LIF-AT2 stem cell niche activity triggers the initiation and progression of the IPF.

1.6 Hallmarks of the aging lung

Aging is a natural phenomenon with decreased cellular and physiological functions with altered inter-cellular communications. The hallmarks of aging include epigenetic changes, metabolic changes due to mitochondrial dysfunction causing an increase in oxidative stress, genomic mutations, cellular senescence, and stem cell exhaustion (Bueno, Calyeca, Rojas, & Mora, 2020; Sgalla et al., 2018). Loss of the rMC-AT2 stem cell niche is a key hallmark of the aging lung (Chanda et al., 2021).

A recent study using the organoids model demonstrated that aging highly impacts rMCs. They showed a significant reduction in organoid number and size when young AT2s co-cultured with aged rMCs compared to young. This rMCs niche activity is partially rescued with the inhibition of aged-associated NADPH oxidase 4 (Nox4). Surprisingly, aged AT2 cells not showed any significant influence when co-cultured either with young or old rMCs (Chanda et al., 2021).

Another recent study demonstrated that Cell division control protein 42 homolog (Cdc-42) regulates the differentiation of AT2 cells to alveolar epithelial type 1 (AT1) cells during development. Interestingly, the deletion of *Cdc-42* in AT2 cells at a young age triggered the fibrosis formation from the periphery to the center of the lung with aging. This hallmark was due to AT2s impaired regeneration, which triggered the mechanical stress, and activated latent Tgfβ, a master signaling cascade of IPF (Wu et al., 2020).

Interestingly, AT2 stem cell exhaustion associated with AT2s senescence is observed in human IPF patients, though what occurs to the LIFs when the AT2s are injured is still unclear. Altered AT2-LIFs communications and interactions due to aging or injury prompt the factors for the induction of the fibrotic phenotype. During the fibrotic state, they undergo collaterally damage and activate the resident fibroblast by pro-fibrotic factors such as TGFβ (Parimon, Yao, Stripp, Noble, & Chen, 2020; Yao et al., 2021).

1.7 LIFs differentiate and contribute to the aMYFs pool during fibrosis

Our recent studies using mice models showed that LIFs differentiate and significantly contribute to the pool of aMYFs during fibrosis. At first, using *Tg(Acta2-CreERT2; tdTomato^{flox}* mice, we showed the pre-existing Vascular smooth muscle cells (VSMC) and Airway smooth muscle cells (ASMC) do not contribute to aMYFs during fibrosis. However, a massive contribution was seen from the cells that acquire *Acta2* expression during the fibrosis formation (El Agha, Moiseenko, et al., 2017).

Next, by using *Adrp^{CreERT2}*, a LIFs-lineage tracing model, it was shown that LIFs transition and contribute to aMYF pool at the peak of fibrosis. Surprisingly, during fibrosis resolution, the aMYFs, despite undergoing massive apoptosis, acquire a lipogenic program and differentiate back to LIFs (El Agha, Moiseenko, et al., 2017).

Unfortunately, in humans, fibrosis is progressive with no resolution seen like in mouse models. Our study in human IPF lungs identified the reversible LIF to aMYF switch. This study used Metformin, an anti-hyperglycemic drug, in patients with type 2 diabetes. Metformin induced lipogenesis and facilitated lipid droplet formation. The associated signaling molecules for lipid droplet formation, such as *PLIN2* and *Peroxisome*

proliferator-activated receptor gamma (*PPARg*) expression, also increased with the treatment. The lipogenic activity of Metformin is by inducing the expression and secretion of bone morphogenetic protein 2 (BMP2). Activation of BMP2 signaling in aMYFs led to the induction of *PLIN2* expression and lipid droplet formation. In addition, Metformin showed anti-fibrotic activity via AMPK-dependent COL1A1 (Collagen Type I Alpha 1 Chain) inhibition (Kheirollahi et al., 2019) (Figure2).

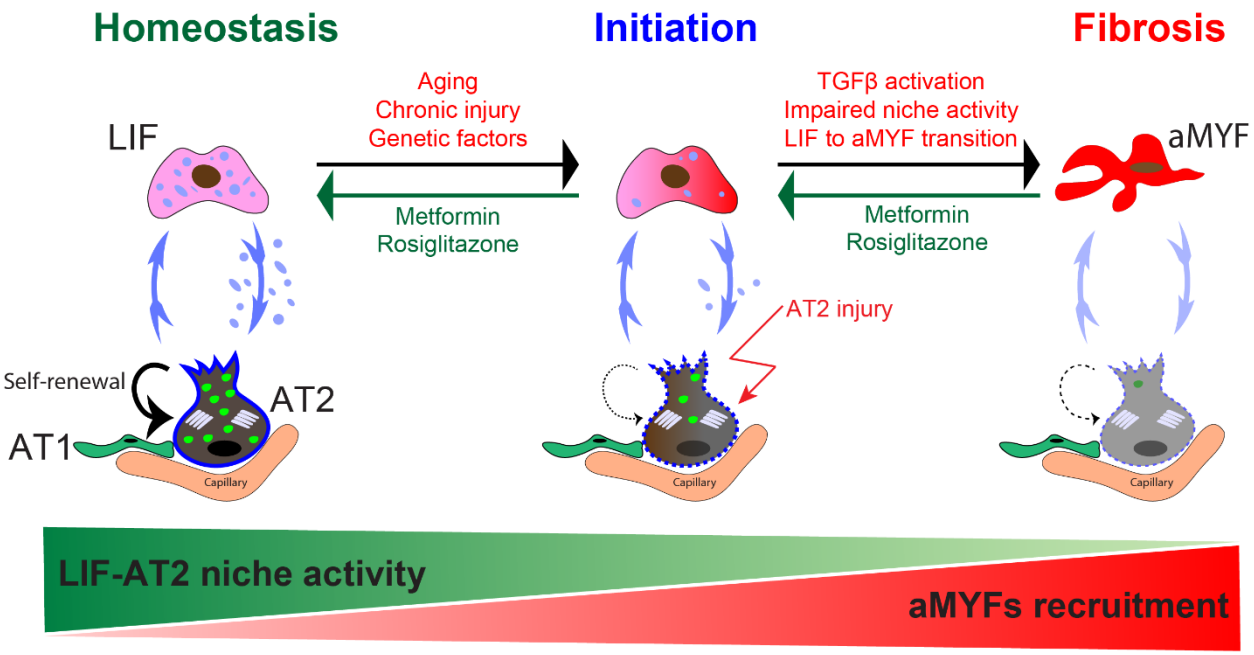

Figure 2: **LIF and AT2 interaction during homeostasis and IPF.**

During homeostasis LIF and AT2 crosstalk is crucial for lipid trafficking and surfactant production. Fgf10 signaling conserves and maintains LIFs activity, which is vital for the stem cell activity of AT2, thereby helping in the self-renewal and maintenance of the AT2s. In contrast, during IPF, loss of AT2s due to aging or injury leads to disruption of LIF-AT2 crosstalk, in due course programming LIFs to aMYFs differentiation with excessive ECM deposition. Metabolic reprogramming by using metformin or rosiglitazone enhances the differentiation of aMYFs to LIFs and helps to retain the LIF phenotype.

1.8 Murine models in IPF

Mouse models are widely accepted and used to study the initiation and progression of pulmonary fibrosis.

Various established mouse fibrosis models are currently in use, which include silica, asbestosis, cytokine overexpression, amiodarone, fluorescent isothiocyanate, radiation-induced, and bleomycin model (Tashiro et al., 2017). However, each model has its advantages and limitations.

The Bleomycin model is most commonly used to study fibrosis in mice. Bleomycin (Bleo) is a chemotherapeutic drug prescribed for cancer patients. Interestingly some patients who received bleomycin developed pulmonary fibrosis as a side effect. The exact mechanism of action of bleomycin is unknown; however, it is believed bleomycin breaks DNA strands and increases reactive oxygen species, thus leading to inflammation, epithelial cell death, and fibroblast activation.

Despite the most commonly used model, this model has limitations, including the variations in fibrosis development between mice. Furthermore, age and gender influence the grade of fibrosis development. Aged male mice are more vulnerable to fibrosis than young males. Additionally, young and old female mice exhibited less fibrosis and mortality than male mice (Redente et al., 2011). In addition, this model is often criticized for the acute development of fibrosis and is capable of fibrosis resolution. However, in humans, fibrosis is chronic with a longer period to develop, and is unfortunately not reversible.

Against the background, we used the Bleomycin model for this study, as it is the best available and most commonly used model to study the development and resolution of the disease.

1.9 Collagen triple helix repeat containing 1 positive aMYFs in IPF

Collagen triple helix repeat containing 1 (Cthrc1) was initially identified in the injured rat carotid arteries due to balloon injury. This novel discovery led to an understanding of the pathogenesis of constrictive vascular remodeling and lumen narrowing. Tgfβ signaling

activates and guides the adventitial fibroblasts to transdifferentiate into aMYFs, eventually developing neointima due to arterial fibrosis with excessive ECM deposition. Interesting *Cthrc1* expression was observed in the adventitia fibroblasts and neointima of injured arteries. This discovery showed Tgfβ signaling is a crucial regulator of *Cthrc1* expression (Pyagay et al., 2005). Furthermore, Cthrc1 activates Tgfβ signaling by enhancing the Smad2/Smad3 phosphorylation. The activated Smad2/3 dimer forms a complex with Smad4, and then the complex translocates into the nucleus for modulating Col1a1 expression and deposition. In contrast, studies show that Cthrc1 inhibits TGFβ signaling by Smad2/Smad3 degradation (LeClair & Lindner, 2007; Myngbay, Manarbek, Ludbrook, & Kunz, 2021).

Wingless related integration site (Wnt) signaling is another important mediator in the progression of fibrosis; studies show that Wnt ligands and its essential regulatory protein β-catenin are elevated in pulmonary fibrosis. A recent study proposed that Sonic hedgehog (Shh) signaling act as an upstream of the Wnt signally during fibrosis. Shh signaling mediated Wnt10a upregulation which enhanced the transition of fibroblasts to aMYFs. Furthermore, various studies showed the inhibition of Wnt signal attenuated and reversed pulmonary fibrosis (Cao et al., 2020; Henderson et al., 2010; Piersma, Bank, & Boersema, 2015). Moreover, studies propose that Cthrc1 modulates Wnt signaling in various organ cancers (Mei, Zhu, Zhang, & Wei, 2020; E. H. Park et al., 2013).

In the IPF, pirfenidone attuned the rhCTHRC1 mediated increase of the ACTA2 and fibronectin expression (Jin et al., 2019). However, in another study, Cthrc1 knock-out mice showed elevated Tgfβ and fibrosis levels; this effect might be due to the use of global knock-out mice instead of cell-specific knock-out mice (Binks, Beyer, Miller, & LeClair, 2017).

Given the background, a new population of cells that are positive for Cthrc1 has been identified during fibrosis in the lung. This population is colocalized with the aMYFs in the fibrotic regions of the lung and expresses high levels of collagen and Acta2. Human IPF lungs also showed the presence of Cthrc1 positive cells in the fibrotic foci with high levels of collagen expression (Tsukui et al., 2020). This study suggested that Cthrc1 cells could be considered a new marker for the aMYFs in fibrosis.

2. Objectives

IPF is a chronic and progressive lung disease with incurable treatment. Currently, available medications can only inhibit disease progression with no therapeutic function. However, long-term use of currently available medications shows resistance and finally leads to lung failure. Despite advances in IPF research, with numerous studies proposing and identifying various molecular pathways associated with the initiation and progression of the disease, it is still a challenging task to develop novel therapeutic interventions.

These challenging concerns are due to activated myofibroblasts of the heterogeneous population with multiple sources of origin. Therefore, better characterization of these heterogeneous populations and understanding of the molecular cues associated with the activation and differentiation from native state to activated myofibroblasts will help to explore novel therapeutic interventions for IPF.

Our recent studies using lineage-labeled mice models proposed that the LIFs are one of the sources of aMYFs. Further, in humans, we showed that Metformin reversed the aMYFs to LIF phenotype and displayed anti-fibrotic activity.

Given the background, in this study, two-month-old *Tg(Acta2-CreERT2); tdTomato*^{flox} mice were used to label *Acta2*$^{positive(pos)}$ cells before or after bleomycin administration. Using scRNA-seq, the origin and fate of *Acta2*^{pos} cells converging on the aMYFs lineage were analyzed at the peak of fibrosis at day 14 and during resolution at day 60.

The aims of this study are as follows:

1) Identification of the anatomical locations of the Acta2^{pos} cells in the lung during homeostasis
2) Characterization of the origin of Cthrc1^{pos} aMYFs and their heterogeneity during fibrosis formation
3) Understanding the fate of the Cthrc1^{pos} aMYFs during resolution
4) Better characterization of the LIF-to-aMYF reversible switch during fibrosis formation and resolution

3. Materials and Methods

3.1 Ethical aspects and mice

All animal experiments were performed according to the approved protocols by the Regierungspraesidium Giessen, the animal ethics committee of the University of Giessen (permit numbers: G57/2019–No.974_GP and G26/2020–No.1002_GP).

All animals were housed under specific pathogen-free (SPF) conditions and a maximum of 5 animals were housed in a single cage. The cages were placed in an individually ventilated cage system and supplemented with bedding and nesting material, with unlimited access to food and water. The room environment was maintained under controlled conditions with 12 hours of dark/light cycle at 22 °C and 40-70% humidity.

Tg(Acta2-CreERT2) mice (STOCK_*Tg(Acta2-cre/ERT2)12Pcn*) (kind gift from Dr. Pierre Chambon, University of Strasbourg, France) were crossed with *td-Tomato*^{flox} (*B6;129S6-Gt (ROSA) 26Sortm9(CAG-tdTomato)Hze/J* (Jackson lab, 007909) to generate tamoxifen-inducible reporter mice.

3.2 Genotyping

Mice tail biopsies were digested in 200 µl Viagen including 2 µl proteinase K at 55°C on a thermomixer comfort overnight, and then the reaction was stopped at 85°C for 40 min. Next, PCR was employed to amplify DNA using specific primers (Table 1). The PCR product of the samples was then analyzed using a QIAxcel capillary gel electrophoresis instrument (Qiagen, 9002123).

Table 1. Protocols for genotyping and band size of PCR products

Mouse Line	Expected band size		Primer sequence	PCR Protocol		
	WT	Mutant		Step	Temp. (°C)	Time (sec)
Acta2-CreERT2	------	349 bp	1) ATT TGC CTG CAT TAC CGG TC 2) ATC AAC GTT TTG TTT TCG GA	1	94	180
				2	94	30
				3	51.7	60
				4 repeat Step 2-4 35 times total	72	60
				5	72	120
				6	4	hold
tdTomato^{flox}	297 bp	196 bp	1) CTG TTC CTG TAC GGC ATG G 2) GGC ATT AAA GCA GCG TAT CC 3) CCG AAA ATC TGT GGG AAG TC 4) AAG GGA GCT GCA GTG GAG TA	1	94	180
				2	94	20
				3	61	30
				4 repeat Step 2-4 35 times total	72	30
				5	72	2
				6	4	hold

3.3 Bleomycin instillation

8- 12 weeks-old female mice were subjected to an intratracheal (I.T.) instillation (150 µl) of either saline or bleomycin 2 U/kg body weight (Bleomedac, PNZ-02411351) using a micro-sprayer (Penn-Century, Inc.). Post intratracheal instillation, lungs were harvested at days 14, 30, and 60 for analysis.

3.4 Tamoxifen administration

Tamoxifen (Sigma, T5648-5G) was dissolved in corn oil (vehicle), and mice were intraperitoneally (I.P.) injected with a dose of 0.1 mg/g body weight. Saline and Bleo-Tam mice were subjected to four successive tamoxifen injections at days 5, 7, 9, and 11 *after* saline or bleomycin instillation, respectively. Tam-Bleo mice were subjected to three consecutive tamoxifen injections at days -18, -16, and -14 *before* bleomycin instillation.

3.5 Immunofluorescence staining

Lungs were perfused with PBS, and harvested lungs were fixed with 4% PFA and dehydrated with Ethanol. The fixed lungs were then embedded in paraffin blocks.

Five-µm-thick paraffin slices were deparaffinized and rehydrated by

Reagent/solution	Time (minutes)
Xylol	10
Xylol	10
100% Ethanol	5
100% Ethanol	5
95% Ethanol	5
70% Ethanol	5
50% Ethanol	5
30% Ethanol	5
Milli-Q water	5

After rehydration, the slides were subjected to antigen retrieval by placing them in citrate buffer and boiling them for 15 min in a cooker. Following cooking, slides were cooled on ice for 20 minutes and washed with PBST three times. Finally, the tissues were blocked with *3% BSA + 0.4% Triton-X in PBS* for 1 hour at room temperature.

Acta2 and Red fluorescent protein (RFP) staining:

Following blocking, slides were incubated overnight with primary antibodies: anti-Acta2 (1:250, Sigma, F3777), and anti-RFP (1:250, Invitrogen, R10367) in *1.5% BSA + 0.2% Triton-X in PBS*, at 4°C overnight. After washing, they were incubated with a secondary antibody (1:500) against RFP in *1.5% BSA + 0.2% Triton-X in PBS,* for 1 hour at room temperature and finally mounted with ProLong Gold Antifade Reagent containing DAPI (Molecular Probes, P36935). To quantify tdTomato^{positive} (tdTom^{pos}) cells, nine independent fibrotic 63x fields per group were quantified from three independent mice lungs.

Acta2, RFP and Cthrc1 staining:

Following blocking, slides were then incubated overnight with primary antibodies: anti-Acta2 (1:250, Sigma, F3777), anti-RFP (1:250, Invitrogen, R10367), and anti-Cthrc1 (1:100, R&D Systems, AF5960) at 4°C overnight. After washing, they were incubated with secondary antibodies (1:500) against RFP and Cthrc1 for 1 hour at room temperature and finally mounted with ProLong Gold Antifade Reagent containing DAPI (Molecular Probes, P36935).

Acta2, Sftpc and Cthrc1 staining:

Following blocking, slides were then incubated overnight with primary antibodies: anti-Acta2 (1:250, Sigma, F3777), anti-Cthrc1 (1:100, R&D Systems, AF5960), and anti-Pro-Spc (1:500, Millipore, AB3786) at 4°C overnight. After washing, they were incubated with secondary antibodies (1:500) against Pro-Spc and Cthrc1 for 1 hour at room temperature and finally mounted with ProLong Gold Antifade Reagent containing DAPI (Molecular Probes, P36935).

3.6 Hematoxylin and eosin staining

Lungs were perfused with PBS, and harvested lungs were fixed with 4% PFA and dehydrated with Ethanol. The fixed lungs were then embedded in paraffin blocks.

Five-µm-thick paraffin slices were deparaffinized and rehydrated by

Reagent/solution	Time (minutes)
Xylol	10
Xylol	10
100% Ethanol	5
100% Ethanol	5
95% Ethanol	5
70% Ethanol	5
50% Ethanol	5
30% Ethanol	5
Milli-Q water	5

After rehydration, the sections were stained with hematoxylin (Roth, T865.2) for 2 minutes and washed with running tap water for 10 minutes. They were then stained with eosin (Thermo Fisher Scientific, 6766007) for 1 min. Following staining, sections were dehydrated and mounted.

3.7 Lung dissociation and Fluorescence-activated cell sorting (FACS)

Mice were sacrificed, and the lungs were perfused with 10 mL PBS through the heart. Lungs were finely chopped and digested in collagenase type IV (0.5%, Gibco 17104-019) at 37°C for 45 minutes. After digestion, the cell suspension is passed through 70 and 40 µm cell strainers. The single-cell suspension was centrifuged and stained with antibodies.

For tdTom^{pos} cells sorting, the pellet was resuspended with anti-CD31 (Alexa Fluor 488-conjugated 1:100, Biolegend, 102514), anti-CD45 (Alexa Fluor 488-conjugated 1:100, Biolegend, 103122), anti-EpCAM (APC-Cy7-conjugated 1:50, Biolegend, 118217) antibodies at 4°C for 20 min. After washing, the cell suspension was stained with SYTOX^{TM} (Invitrogen, S34857), and sorting was carried out using FACSAria III cell sorter (B.D. Biosciences).

For Sca1^{pos} cells sorting, the pellet was resuspended with anti-CD31 (Alexa Fluor 488-conjugated 1:100, Biolegend, 102514), anti-CD45 (Alexa Fluor 488-conjugated 1:100, Biolegend, 103122), anti-EpCAM (APC-Cy7-conjugated 1:50, Biolegend, 118217) and anti-Sca1 (pacific blue-conjugated 1:50, Biolegend, 108120) antibodies at 4°C for 20 minutes. After washing, the sorting was carried out using a FACSAria III cell sorter (B.D. Biosciences).
Data were analyzed using FlowJo software (FlowJo, LLC).

3.8 Generation and analysis of the scRNA-seq data

Sorted tdTom^{pos} cells were centrifuged and resuspended in 0.04% ultrapure BSA (Invitrogen, 01266574) in PBS for optimal cell concentration. Then, 9,000 cells were loaded into the Chromium Controller (10x Genomics). The cDNA libraries were prepared according to the manufacturer's instructions. Sequencing was performed by Nextseq2000 (Illumina, Inc.), and reads were aligned against a custom mouse reference genome (mm10) and counted by STARsolo.

All downstream analyses were carried out with the Seurat R package (v4.1.0) (Hao et al., 2021). The counts matrix of each sequenced sample was loaded as Seurat objects. Using UMIs and mitochondrial content arbitrary thresholds, low-quality cells were discarded. Then, saline, Tam-Bleo d14, Bleo-Tam d14 and Bleo-Tam d60 samples were integrated using LIGER workflow (rliger R package v1.0.0) (Welch et al., 2019). Briefly, all samples were first merged into one Seurat object, and all counts were log-normalized. The 2,000 most variable features in the aggregated dataset were scaled but not centered for each sample individually. Next, integrative non-negative matrix factorization (iNMF) was run on each sample using the RunOptimizeALS function with the following parameters: k = 50, lambda = 3. Clusters of the shared factor neighborhood graph were quantile-normalized using the RunQuantileNorm function with default parameters. Clusters were obtained using Louvain community detection on the 50 first dimensions of the iNMF-reducted space using k.param =10 and visualized in two dimensions using UMAP. According to UMIs content and differentially expressed genes in each cluster, clusters corresponding either to remaining low-quality cells or non-mesenchymal cells (immune and endothelial cells) were removed. The complete integration process was rerun on the subset of kept cells with the same parameters. Finally, obtained clusters were annotated according to the expression of their specific markers. Subclusters of Cthrc1^{pos} aMYFs, adventitial and peribronchial fibroblasts were also identified in this reduced dimensional space computed from all samples. In contrast, alveolar fibroblast subclusters were obtained in each subset of sample pairs. UMAP plots were also rerun on each particular subset using the same first 50 iNMF dimensions computed on the complete dataset.

For the detailed analysis of Tam-Bleo d14 and Tam-Bleo d60 samples, both samples were first integrated as described above. Then, the obtained clusters were annotated by label transfer using the previously integrated dataset as a reference. Transfer anchors between the two datasets were identified in PCA-reducted space using the first 50 principal components. Then, the corresponding cell type of each cell from the query dataset was predicted using the TransferData function.

Marin Truchi (*Université Côte d'Azur, CNRS, IPMC, Sophia Antipolis, Valbonne, France*) carried out the bioinformatic analysis on the generated mouse samples.

Olivier Mauduit (*Department of Molecular Medicine, The Scripps Research Institute, La Jolla, CA, USA*) carried out the data mining and bioinformatic analysis on the human IPF samples.

3.9 Alveolosphere assay

6-8 weeks old C57BL6 mice lungs were perfused with 10 mL PBS through the heart and inflated intratracheally with 3 mL dispase (5000 Units, Corning, 354235). The inflated lungs were digested in an additional 3 mL dispase solution at room temperature for 30 minutes. Following digestion, the cell suspension is passed through 70 and 40 µm cell strainers, and the tissue is centrifuged. Pellet was resuspended with anti-CD31 (Alexa Fluor 488-conjugated 1:100, Biolegend, 102514), anti-CD45 (Alexa Fluor 488-conjugated 1:100, Biolegend, 103122), anti-EpCAM (APC-Cy7-conjugated 1:50, Biolegend, 118217). To isolate and sort mature AT2 cells from EpCAM population, we additionally stained with Lysotracker (Invitrogen™ L7528).

Sorted 50,000 $Sca1^{pos}$ resident mesenchymal cells (rMCs) from *Tg(Acta2-CreERT2)/+; tdTomato^{flox}* mice and 5,000 $Lysotracker^{pos}$ epithelial cells from C57BL/6J mice, were mixed and reconstituted in 100 µL media, followed by addition of 100µL ice cold Matrigel (Corning, 356231). First, the 1:1 mixture was transferred to 24-well 0.4 µm Transwell inserts (Greiner bio-one, 662641) and incubated at 37°C for 15 min for Matrigel polymerization. Next, 500 µL of media [sorting media plus 1% ITS (Gibco, 41400-045)] was added to each well and incubated at 37°C in 5% CO_2 for 14 days. The medium was changed every 2 days.

3.10 Statistical analysis

Graph assembly and statistical analyses were carried out using GraphPad Prism Software. To compare the two groups, unpaired, two-tailed t-tests were used. For comparisons involving more than two groups, one-way ANOVA with post hoc Newman–Keuls multiple comparisons test was used. Values of $P<0.05$ were considered statistically significant. All data are presented as mean ± SEM.

4. Results

4.1 Lineage tracing of *Acta2^{pos}* cells in healthy and fibrotic mouse lungs.

Six-to-eight-week-old *Tg(Acta2-CreERT2)/+; tdTomato^{flox}* female mice were subjected I.T. with a bleomycin dose sufficient to induce moderate fibrosis. Tamoxifen was administered before (Tam-Bleo condition) or after bleomycin (Bleo) administration (Bleo-Tam condition) to examine the fate of *Acta2^{pos}* cells during fibrosis formation (Figure 3a). Experimental and control mice (saline condition) were analyzed on day 14, representing the peak of fibrosis. Hematoxylin Eosin staining on the corresponding isolated lungs demonstrated the presence of fibrotic areas on day 14 following injury (Figure 3b, c), and Ashcroft scoring (Ashcroft, Simpson, & Timbrell, 1988) indicated a mild-to-moderate injury with no significant difference between Tam-Bleo and Bleo-Tam mice (Figure 3d). Next, we visualized the lineage-traced *Acta2^{pos}* cells by IF using antibodies against Rfp and Acta2 (Figure 3e, f). In the saline condition, we identified tdTomato (tdTom) expression in cells located within the peribronchiolar and vascular regions with most of these cells co-expressing high levels of Acta2 and therefore corresponding to the ASMCs and VSMCs (Figure 3e). Interestingly, we also found tdTom^{pos} cells with low levels of Acta2 close to the peribronchial regions and in the parenchyma (Figure 1f). Then, we examined tdTom^{pos} cells in Bleo-treated mice. In Tam-Bleo, these cells only showed a minor contribution to the fibrotic areas, supporting the claim that pre-existing *Acta2^{pos}* cells are not significant contributors to aMYFs. However, in Bleo-Tam conditions, where the *Acta2^{pos}* cells are labeled after injury, we found significant enrichment of tdTom^{pos} cells in the fibrotic regions (Figure 3e, f). The quantification of tdTom^{pos} cells over total DAPI^{pos} cells in the fibrotic areas confirmed this observation (Figure 3g) (Tam-Bleo: 16% ± 1.9% and Bleo-Tam: 53% ± 8.1%, P=0.01)

Flow cytometry was used to quantify the percentile of tdTom^{pos} cells out of the CD45/CD31/EpCAM triple-negative resident mesenchymal cells (rMCs) in saline, Tam-Bleo, and Bleo-Tam (Figure 3h). SYTOX^{TM} staining was used to exclude dead cells from the analysis. We found a statistically significant increase in the abundance of tdTom^{pos} cells in Bleo-Tam (11% ± 2.3%) vs. Tam-Bleo (5.8% ± 0.59%) (P=0.04) (Figure 3i)

supporting our previous finding that most of the *Acta2*^{pos} cells arising following Bleo injury arise from *Acta2*^{neg} cells (El Agha, Moiseenko, et al., 2017).

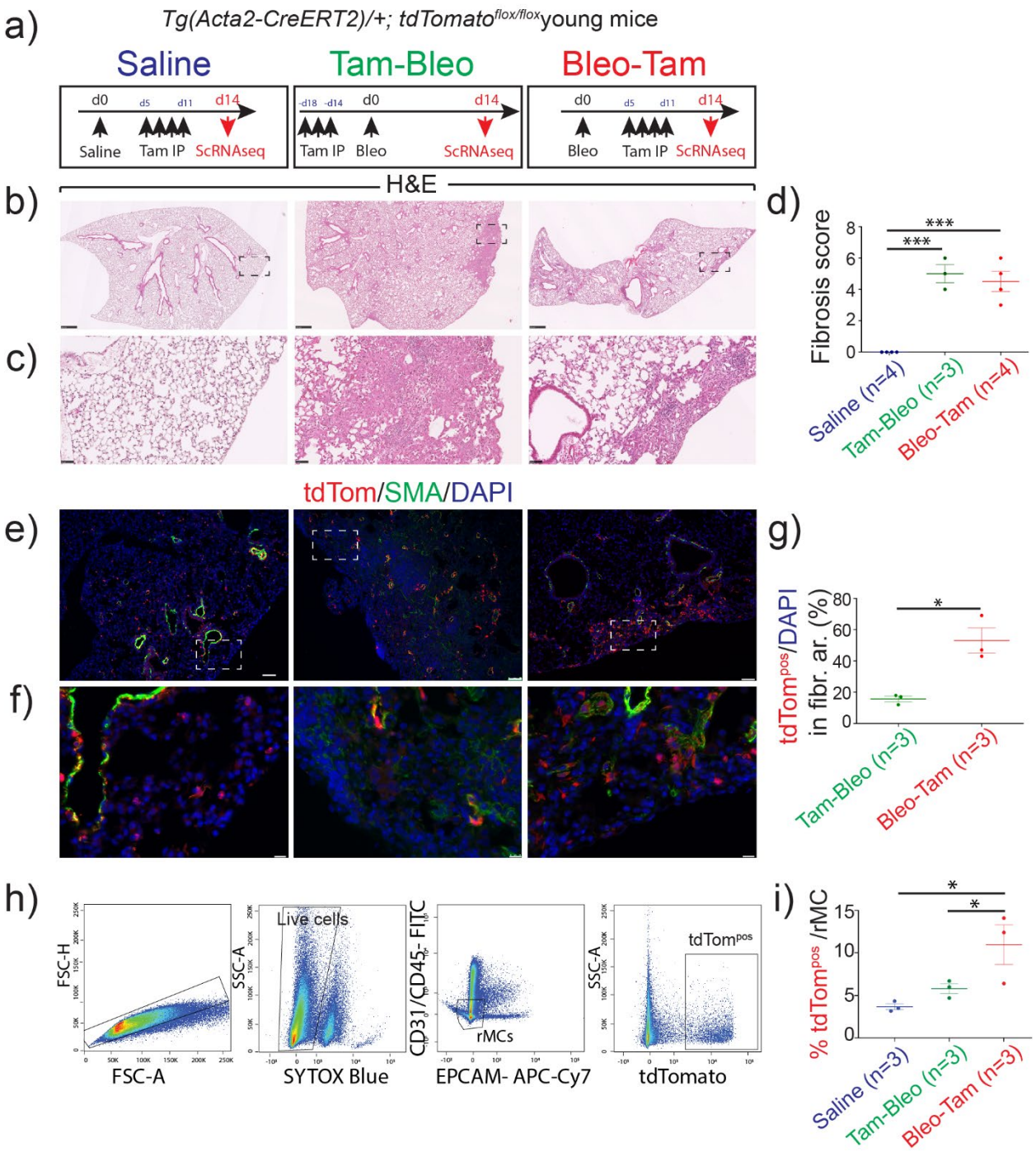

Figure 3: **Lineage tracing of *Acta2^{pos}* cells in saline, Tamoxifen-Bleomycin and Bleomycin-Tamoxifen conditions.**

a) 8-12 weeks-old female *Tg(Acta2-CreERT2)/+;tdTomato^{flox}* mice are used to lineage label *Acta2^{pos}* cells in saline, Tamoxifen-Bleomycin and Bleomycin-Tamoxifen conditions. Control and experimental lungs are collected at day14 following saline or bleomycin administration. **b and c)** Corresponding low and high magnification of H&E staining showing fibrosis formation at day 14 following bleomycin injury both in Tam-Bleo and Bleo-Tam. **d)** Ashcroft score confirming mild to moderate fibrosis formation upon fibrosis injury Saline 0 ± 0 score (n=4), Tam-Bleo 5 ± 0.58 score (n=3), Bleo-Tam 4.5 ± 0.65 score (n=4). **e and f)** Corresponding low and high magnification of IF staining against Rfp, Acta2 and DAPI, indicating the presence of tdTom^{pos} cells in the bronchiolar region as well as in the alveolar region in saline conditions. Note the minor contribution of tdTom^{pos} cells in the fibrotic region in Tam-Bleo conditions and the presence of abundant tdTom^{pos} cells in the fibrotic region in Bleo-Tam conditions. **g)** Quantification of the percentile of tdTom^{pos} /total DAPI in the fibrotic areas of Tam-Bleo 16% ± 1.9% (n=3) and Bleo-Tam 53% ± 8.1% (n=3). **h)** Gating strategy to sort lineage-labeled tdTom^{pos} cells. **i)** Representative Quantification of sorted tdTom^{pos} cells from Saline (n=3), Tam-Bleo (n=3), Bleo-Tam (n=3) out of resident mesenchymal cells (rMCs). No significant difference was observed between Tam-Bleo 5.8% ± 0.59% and Saline 3.7% ± 0.35% (P value: 0.32). By contrast, there is a stark increase in Bleo-Tam 11% ± 2.3% versus Tam-Bleo 5.8% ± 0.59% (P value: 0.04) or between Bleo-Tam and Saline (P value: 0.02). Scale bar: b- 500µm, c-50µm, e-75µm and f- 10µm. Statistical analysis was performed using: (d and i)- one-way ANOVA with Newman–Keuls post hoc test for multiple comparisons; (g)- unpaired two-tailed t-test. *: $p<0.05$; ***: $p<0.001$.

4.2 *Acta2*^{pos} cells contribute to multiple lineages in homeostasis condition but with low commitment to the *Cthrc1*^{pos} aMYF lineage.

Lineage-labeled *Acta2*^{pos} (tdTom^{pos}) cells were sorted from saline and Tam-Bleo lungs at day 14 by negative gating for CD31, CD45, and EpCAM (Figure 3h). Then, 9,000 cells per condition were loaded for scRNA-seq. After quality control (Figure 4a), a total of 2,182 cells were recovered for the saline group and 7,125 cells for the Tam-Bleo group (Figure 4b). We found 18 different subclusters, including alveolar fibroblasts (Al1,2), adventitial fibroblasts (Ad1,2), peribronchial fibroblasts (Pb1-3) as well as smooth muscle cells (SMC)/Pericytes and Cthrc1 fibroblasts (Ct1-Ct4) (Figure 5a). Figure 5b displays the heatmap with the corresponding highly expressed genes for each cluster. The proportion of alveolar fibroblasts (Al1,2) and adventitial fibroblasts (Ad1,2) was decreased while that of peribronchial fibroblasts (Pb1-3) was increased in Tam-Bleo vs. saline (Figure 5c).

The Prolif. Cthrc1F. and the Cthrc1F. clusters (Ct1-Ct4) represented 1.7% of the total cells in the saline vs. 3.8% in Tam-Bleo, confirming the minimal contribution of pre-existing *Acta2*^{pos} lineage to aMYFs (Figure 5c). Interestingly, among *Cthrc1*^{pos} fibroblasts, *Cthrc1* was found to be already expressed in cluster Ct2 in saline, and its expression was amplified upon Bleo injury. Lower levels of *Cthrc1* expression were also observed in clusters Ct3 and Ct4 upon Bleo injury (Figure 5d).

Next, we carried out a refined analysis for the *Cthrc1*^{pos} cluster (Figure 5e). Taking into consideration the combined number of cells in saline and Bleo samples for each subcluster, we concluded that Ct2 was the most abundant cluster (45.7%), followed by Ct1 (27.6%), Ct3 (23.6%) and Ct4 (3.1%) (Figure 5e). Examination of the relative number of cells for each *Cthrc1* ^{pos} cluster arising from saline indicates that the vast majority were found in Ct1 and Ct2 only, with 55% and 39% of total cells present in saline. Interestingly, Ct2 found in saline is also very close to the main signature of Ct1 (Figure 5f), indicating that this subcluster is specific of homeostatic conditions. However, in the context of Bleo, the proportion of cells in Ct1 decreased (from 55% to 24%). The Ct2 cells displaying a Ct1 signature in saline acquire a Ct2 signature upon Bleo injury, which is enriched in *Cthrc1* expression.

Next, we carried out a refined analysis for the alveolar fibroblast cluster. This cluster can be subdivided into Al1 and Al2 (Figure 5h). Al2 represents 36.5% of the cells in the alveolar fibroblast cluster. Figure 5i displays the heatmap with the corresponding differentially highly expressed genes for Al1 and Al2 in saline and Bleo. Al1 in saline displays dispersed expression of both Al1 and Al2 alveolar fibroblast signature. Upon Bleo treatment, the expression was increased and polarized to Al1 signature. Al2 in saline is enriched with alveolar fibroblast markers such as *Scube2*, *Ces1d,* and *Npnt.* Interestingly, upon Bleo treatment, Al2 displayed dispersed expression by acquiring Al1 signature, with a decreased expression of its native signature.

We then evaluated the expression of a LIF signature, composed of 17 genes identified through a literature search (X. Liu et al., 2021) in the different clusters. Of note, an enrichment of this signature was found in Ct1. Furthermore, this signature was also enriched in Al2 (Figure 5k). Interestingly, this LIF signature thus appears to be globally reduced in Bleo vs. Saline.

Altogether, our data indicate that the saline lung already contains a primed pro-fibrotic niche with the existence of lineage-labeled *Cthrc1*^{pos} cells. The alveolar fibroblast cells positive for *Acta2* expression are hypothesized to contribute to the *Cthrc1*^{pos}/aMYF pool during fibrosis formation.

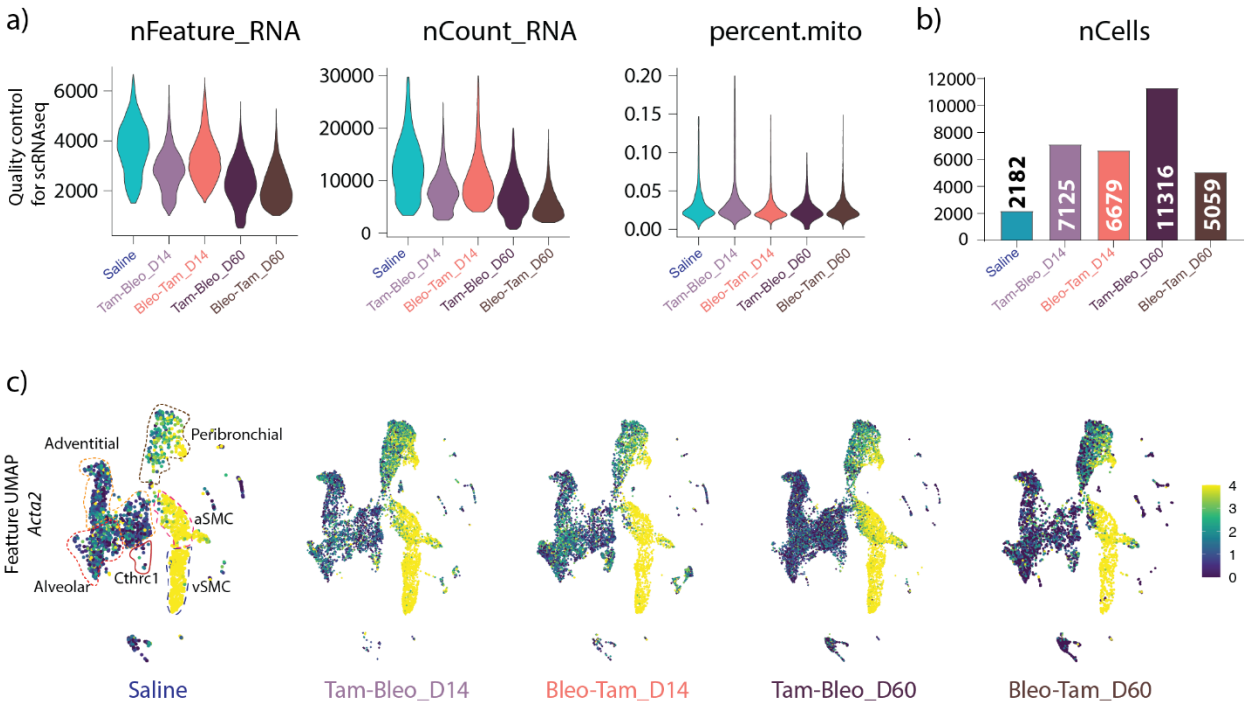

Figure 4: **Quality control of scRNA-seq data sets.**

a) Violin plots showing quality control RNA features, RNA count and mitochondrial RNA for saline, Tam-Bleo and Bleo-Tam at corresponding time points **b)** Number of cells recovered after quality control and used for the data analyses. **c)** Corresponding Feature plots of *Acta2* expression

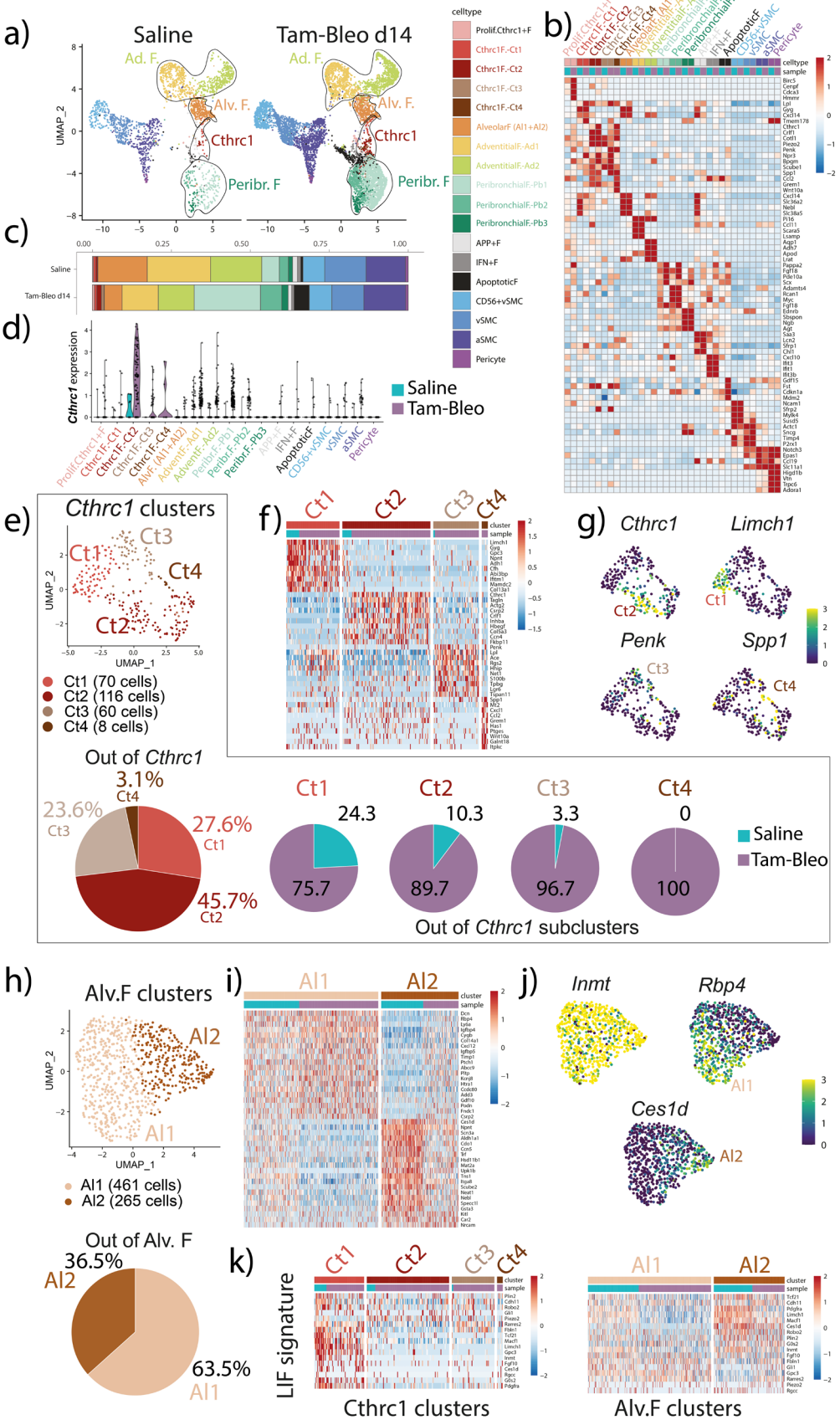
a)
Saline
Tam-Bleo d14
Ad. F.
Alv. F.
Cthrc1
Peribr. F
UMAP_2
UMAP_1
celltype
Prolif.Cthrc1+F
Cthrc1F.-Ct1
Cthrc1F.-Ct2
Cthrc1F.-Ct3
Cthrc1F.-Ct4
AlveolarF (Al1+Al2)
AdventitialF.-Ad1
AdventitialF.-Ad2
PeribronchialF.-Pb1
PeribronchialF.-Pb2
PeribronchialF.-Pb3
APP+F
IFN+F
ApoptoticF
CD56+vSMC
vSMC
aSMC
Pericyte
b)
c)
Saline
Tam-Bleo d14
d)
Cthrc1 expression
Saline
Tam-Bleo
e)
Cthrc1 clusters
Ct1
Ct2
Ct3
Ct4
Ct1 (70 cells)
Ct2 (116 cells)
Ct3 (60 cells)
Ct4 (8 cells)
Out of Cthrc1
3.1%
23.6%
27.6%
45.7%
f)
cluster
sample
g)
Cthrc1
Limch1
Penk
Spp1
Out of Cthrc1 subclusters
24.3
10.3
3.3
0
75.7
89.7
96.7
100
Saline
Tam-Bleo
h)
Alv.F clusters
Al1
Al2
Al1 (461 cells)
Al2 (265 cells)
Out of Alv. F
36.5%
63.5%
i)
j)
Inmt
Rbp4
Ces1d
k)
LIF signature
Cthrc1 clusters
Alv.F clusters

Figure 5: ***Acta2^{pos}* cells contribute to multiple lineages in saline and their labeling before bleomycin injury indicates their minimal commitment to the *Cthrc1^{pos}* myofibroblast lineage.**

a) Integrated UMAP of *Acta2^{pos}* cells isolated from saline and Tam-Bleo lungs at day 14 post-bleo injury showing 18 distinct clusters including alveolar fibroblasts, peribronchial fibroblasts, adventitial fibroblasts and *Cthrc1^{pos}* myofibroblasts. **b)** Heatmap showing genes enriched for each cluster. **c)** Distribution of the different clusters in saline and Tam-Bleo at day 14. Note that the *Cthrc1^{pos}* myofibroblasts already exist in saline and are minimally amplified in Tam-Bleo. The alveolar fibroblasts, adventitial fibroblasts are decreased in Tam-Bleo while the peribronchial fibroblasts are increased. **d)** Violin plot for *Cthrc1* expression indicates that the Ct2 cluster displays the highest expression level. **e)** integrated UMAP of the Cthrc1 clusters from saline and Tam-Bleo lungs. Ct2 represents 45.7% of the overall *Cthrc1^{pos}* cells. *Cthrc1^{pos}* cells are amplified in the context of fibrosis formation. **f)** Heatmap showing the main differentially expressed genes for each *Cthrc1* subclusters. Note that Ct1 contains *Limch1*, a canonical LIF marker. The signature of this cluster is not significantly impacted by bleomycin. Ct2 in saline is enriched in the Ct1 signature. However, upon bleomycin exposure, this Ct1 signature is lost and an Ct2 signature is increased. The Ct3 signature contains *Hhip* and *Lgr6*, markers of peribronchial fibroblasts. The Ct4 cluster, is only observed in the context of Tam-Bleo and displays high level of the fibrotic marker *Spp1*. **g)** Expression of *Cthrc1*, *Limch1*, *Penk* and *Spp1* on feature plots. **h)** Integrated UMAP of the alveolar fibroblasts subclusters from saline and Tam-Bleo lungs. Note that the Al1 represents 63.5% of the total alveolar fibroblasts cluster. **i)** Heatmap showing the main differentially expressed genes for each alveolar fibroblasts subclusters. Al1 is saline displays both the upper and lower part of the alveolar fibroblasts signature. Upon bleo treatment, the lower part of the signature is decreased and the upper part is increased. Al2 in saline does not express the upper part of the signature. Upon bleo, the upper signature is induced and the lower part is reduced. The lower part of the signature contains *Scube2*, *Ces1d* and *Npnt*. **j)** Expression of LIF markers *Inmt*, *Ces1d* and the differentially expressed gene *Rbp4* on feature plots. **k)** Expression of the LIF signature in the different *Cthrc1* subclusters indicates enrichment in Ct1. This signature is also enriched in Al2 of the alveolar fibroblasts.

4.3 *Acta2*^{pos} cells captured during fibrosis formation (Bleo-Tam condition) massively contribute to the *Cthrc1*^{pos} aMYF lineage.

Next, lineage-labeled *Acta2*^{pos} cells captured during fibrosis formation (Bleo-Tam condition) were isolated at day 14 and compared to *Acta2*^{pos} cells isolated from saline-treated lungs (Figure 5). After quality control (Figure 4a), we recovered a total of 6,679 cells (Figure 4b).

The UMAP visualization of the integrated analysis showed 18 distinct clusters, including a highly abundant *Cthrc1* ^{pos} cluster (Figure 6a). Figure 6b shows the heatmap for the genes enriched for each cluster. The distribution of the different clusters in saline and Bleo-Tam at day 14 is shown in Figure 6c and supports our initial observation that *Cthrc1*^{pos} myofibroblasts are drastically increased in Bleo-Tam (Figure 5c). We also noted the presence of proliferating *Cthrc1*^{pos} fibroblasts, which correlates with the drastic increase in *Cthrc1*^{pos} cells. Interestingly, the overall percentile of alveolar fibroblasts was not changed, while those of adventitial and peribronchial fibroblasts were decreased and increased, respectively in Bleo-Tam (Figure 6c). Violin plots for *Cthrc1* expression indicated that all *Cthrc1*^{pos} fibroblast subclusters (Ct1-4) express high levels of *Cthrc1* with Ct2 showing the maximum expression (Figure 6d).

Next, we carried out a detailed analysis of the *Cthrc1* ^{pos} clusters from saline and Bleo-Tam lungs (Figure 6e). All *Cthrc1*^{pos} cells distributed within the 4 clusters were amplified in the context of fibrosis formation, the Ct2 representing 35.1% of the overall *Cthrc1*^{pos} cells. Figure 6f shows the heatmap of the most expressed gene markers for each *Cthrc1* subclusters. Interestingly, the Ct1 cluster contains *Limch1* and *Apoe*, two canonical LIF markers. The signature of this cluster is not significantly impacted by bleomycin. Only 2% of cells within the Ct2 originated from saline and possessed an intermediate “mild” Ct1/Ct2 signature. Both Ct4 and Ct3 were only observed in the context of Bleo-Tam. Pathway analysis comparing the different *Cthrc1* subclusters suggests that Ct4 represents the most activated cluster with increased NFκb, Tnfα, Mapk, Egfr, and Vegf signaling compared to the other *Cthrc1* subclusters (Figure 6g).

We also generated a UMAP of the alveolar fibroblast subclusters integrated from saline and Bleo-Tam datasets. Interestingly, our analysis indicates the presence of a newly

formed Al3, which was not present in the previous analysis (Figure 5h). Al3 represents 40.4% of the total alveolar fibroblast cluster (Figure 6h). This new alveolar fibroblast subcluster Al3 is characterized by the expression of the fibrotic markers *Spp1*, *Eln*, *Ltbp2,* and *Sfrp1* (Figure 3) with low expression of the LIF markers *Inmt* and *Ces1d* (Figure 6j). Finally, the expression of the LIF signature in the different *Cthrc1* subclusters indicates enrichment in Ct1. This signature is also enriched in Al2 of the alveolar fibroblasts (Figure 6k).

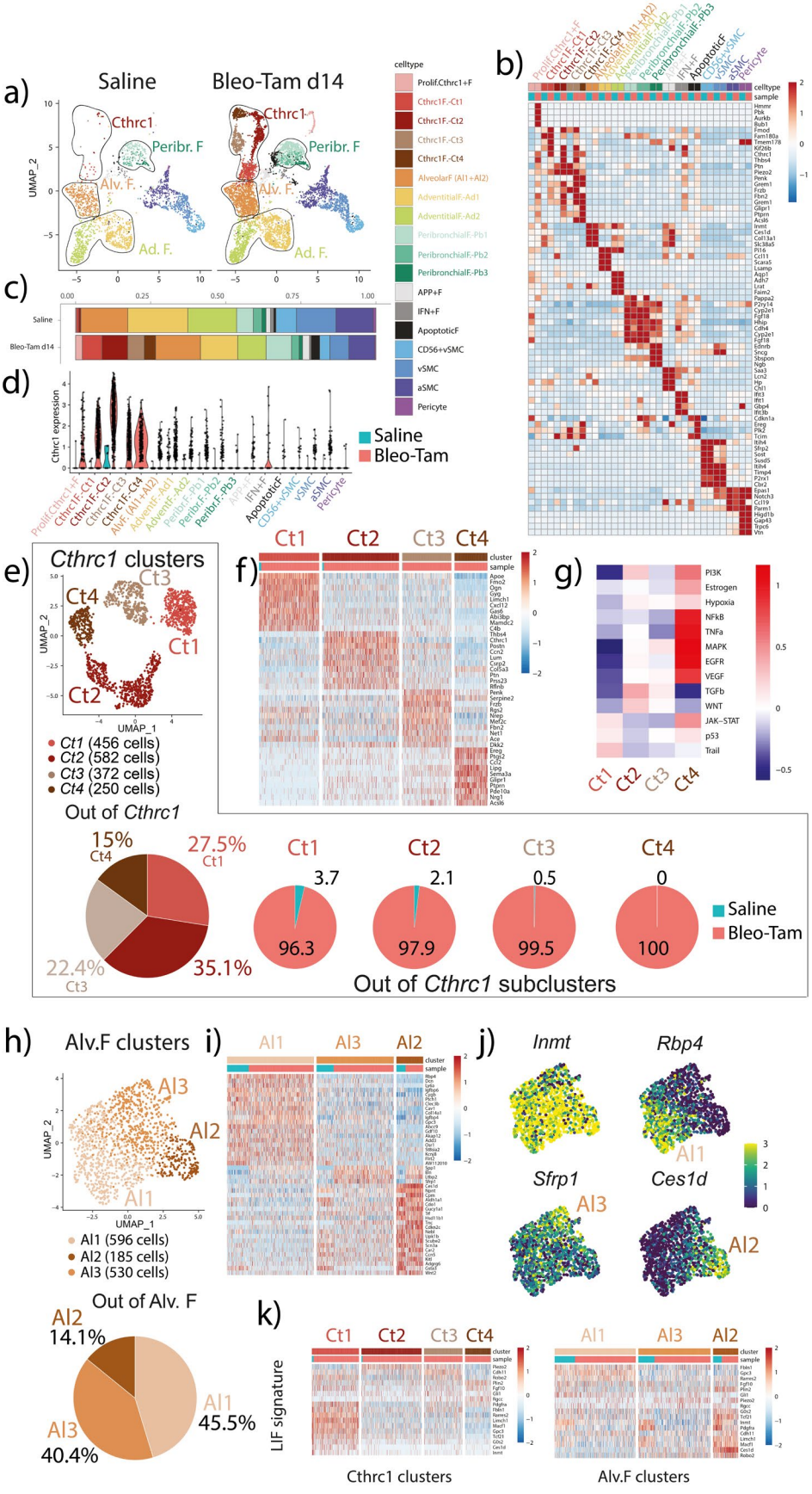
a)
Saline
Bleo-Tam d14
Cthrc1
Peribr. F
Alv. F.
Ad. F.
UMAP_2
UMAP_1
celltype
Prolif.Cthrc1+F
Cthrc1F.-Ct1
Cthrc1F.-Ct2
Cthrc1F.-Ct3
Cthrc1F.-Ct4
AlveolarF (AI1+AI2)
AdventitialF.-Ad1
AdventitialF.-Ad2
PeribronchialF-Pb1
PeribronchialF-Pb2
PeribronchialF-Pb3
APP+F
IFN+F
ApoptoticF
CD56+vSMC
vSMC
aSMC
Pericyte
b)
c)
Saline
Bleo-Tam d14
d)
Cthrc1 expression
Saline
Bleo-Tam
e)
Cthrc1 clusters
Ct1
Ct2
Ct3
Ct4
Ct1 (456 cells)
Ct2 (582 cells)
Ct3 (372 cells)
Ct4 (250 cells)
Out of Cthrc1
15%
Ct4
27.5%
Ct1
22.4%
Ct3
35.1%
f)
cluster
sample
g)
PI3K
Estrogen
Hypoxia
NFkB
TNFa
MAPK
EGFR
VEGF
TGFb
WNT
JAK–STAT
p53
Trail
3.7
96.3
2.1
97.9
0.5
99.5
0
100
Saline
Bleo-Tam
Out of Cthrc1 subclusters
h)
Alv.F clusters
AI1
AI2
AI3
AI1 (596 cells)
AI2 (185 cells)
AI3 (530 cells)
Out of Alv. F
AI2
14.1%
AI1
45.5%
AI3
40.4%
i)
j)
Inmt
Rbp4
Sfrp1
Ces1d
k)
LIF signature
Cthrc1 clusters
Alv.F clusters

Figure 6: ***Acta2^{pos}* cells captured during fibrosis formation (Bleo-Tam condition) massively contribute to the *Cthrc1^{pos}* myofibroblast lineage.**

a) Integrated UMAP of *Acta2^{pos}* cells isolated from saline and Bleo-Tam lungs at day 14 post-bleo injury showing 18 distinct clusters including alveolar fibroblasts, peribronchial fibroblasts, adventitial fibroblasts and *Cthrc1^{pos}* myofibroblasts. **b)** Heatmap showing genes enriched for each cluster. **c)** Distribution of the different clusters in saline and Bleo-Tam at day 14. Note that the *Cthrc1^{pos}* myofibroblasts are drastically increased in Bleo-Tam and include the proliferating *Cthrc1^{pos}* cells. The percentile of alveolar fibroblasts is not changed while Adventitial fibroblasts are decreased in Bleo-Tam while the Peribronchial fibroblasts are increased. **d)** Violin plot for *Cthrc1* expression indicates that all *Cthrc1^{pos}* fibroblast express high level of *Cthrc1* with Ct2 showing the maximum expression. **e)** Integrated UMAP of the *Cthrc1^{pos}* clusters from saline and Bleo-Tam lungs. Ct2 represents 35.1% of the overall *Cthrc1^{pos}* cells. *Cthrc1^{pos}* cells are amplified in the context of fibrosis formation. **f)** Heatmap showing the main differentially expressed genes for each *Cthrc1* subclusters. Note that Ct1 contains *Limch1* and *Apoe*, two canonical LIF markers. The signature of this cluster is not significantly impacted by bleomycin. Ct2 in saline is enriched in the Ct1 signature. However, upon bleomycin exposure, this Ct1 signature is lost and an Ct2 signature is increased. The Ct4, is only observed in the context of Bleo-Tam. **g)** Pathway analysis comparing the different *Cthrc1^{pos}* subclusters suggesting that Ct4 represents the most activated cluster. **h)** Integrated UMAP of the alveolar fibroblasts subclusters from saline and Bleo-Tam lungs. Note that the newly formed Al3 represents 40.4% of the total alveolar fibroblasts cluster. **i)** Heatmap showing the main differentially expressed genes for each alveolar fibroblasts subclusters. Note the presence of new alveolar fibroblast subcluster, Al3, which is characterized by the expression of the fibrotic markers *Spp1*, *Eln*, *Ltbp2* and *Sfrp1*. **j)** Expression of LIF marker *Inmt*, the differentially expressed gene *Rbp4*, the fibrotic gene *Sfrp1* and the LIF marker *Ces1d* on feature plots. **k)** Expression of the LIF signature in the different *Cthrc1* subclusters indicates enrichment in Ct1. This signature is also enriched in Al2 of the alveolar fibroblasts.

4.4 Human IPF lungs display heterogeneity in the *CTHRC1^{pos}* population.

We then analyzed by IF the expression of Cthrc1, Acta2, and Rfp (tdTom^{pos}) in saline and Bleo-Tam lungs at day 14. Low expression of Cthrc1 is detected in the saline lung while a substantial increase in Cthrc1 expression is observed in the fibrotic regions of the Bleo-Tam lungs. Note the overlap between tdTom^{pos} cells, Acta2, and Cthrc1 (Figure 7a). Immunofluorescence for ACTA2, SFTPC, and CTHRC1 was also carried out in human donor and IPF lungs. While CTHRC1 is detected at a low level in SFTPC^{pos} cells in the donor, CTHRC1/ACTA2^{pos} myofibroblasts accumulate in the IPF lungs (Figure 7b).

To analyze the heterogeneity of CTHRC1^{pos} cells in human lungs, we data-mined two previously published/available human IPF datasets (Adams et al., 2020; Habermann et al., 2020). First, using the Adams et al. dataset, we generated an integrated UMAP of donor and IPF lungs with two clusters, fibroblasts (majorly present in donor's lungs) and myofibroblasts (majorly present in IPF lungs). Furthermore, the sub-clustering of the initial two clusters displayed the presence of CTHRC1^{pos} fibroblasts in all fibroblast and myofibroblast populations. Fine resolution of these subclusters was done for better visualization. We selected six different subclusters based on the presence of at least 30% of the cells within this cluster positive for *CTHRC1* regardless of its level of expression (Figure 7c-e).

Interestingly, five subclusters out of six were of myofibroblasts origin and displayed heterogeneity. Cluster 0 belonging to the myofibroblast pool expresses LIF markers. Cluster 3 expresses high levels of fibrotic markers (Figure 7f). Cluster 2 expresses a high level of *ACTA2* expression. Surprisingly, irrespective of the cluster's origin, *LIMCH1* a LIF marker's expression was noticed, with a higher expression in the myofibroblasts pool (Figure 7g). These data suggest that LIFs can differentiate to form pathological aMYFs during fibrosis.

Next, using the Habermann et al. dataset, the four initial fibroblast populations (HAS1^{high} fib., PLIN2+ Fib., fib., MyoFib.) were further subclustered into 8 clusters. The selection of the subclusters was based on the presence of at least 25% of the cells within this cluster positive for *CTHRC1*, regardless of its level of expression (Figure 8a). *CTHRC1* expression was visualized in these clusters using violin plots (Figure 8b) or directly on the

UMAP plot (Figure 8c). As expected, the MyoFib. subclusters (1, 5, 6, and 7) displayed the highest levels of *CTHRC1* expression. Figure 8d shows the corresponding heatmap with the top 10 markers for each cluster. Interestingly, subcluster 1, which belongs to the myofibroblast cluster, expresses LIF markers such as *LIMCH1*, *TCF21*, *MACF1,* and *APOE,* while subcluster 5 expressed a high level of fibrotic markers such as *COL1A1*, *SPARC*, *COL3A1,* and *FN1*. The expression of *ACTA2* as a myofibroblast marker and *LIMCH1* as a LIF marker is shown as a violin plot. *ACTA2* is detected in all the subclusters with a maximal expression in clusters 1, 5, 6, and 7. Supporting a LIF-to-MYF transition, *LIMCH1* was detected almost exclusively in MyoFb. clusters (Figure 8e).

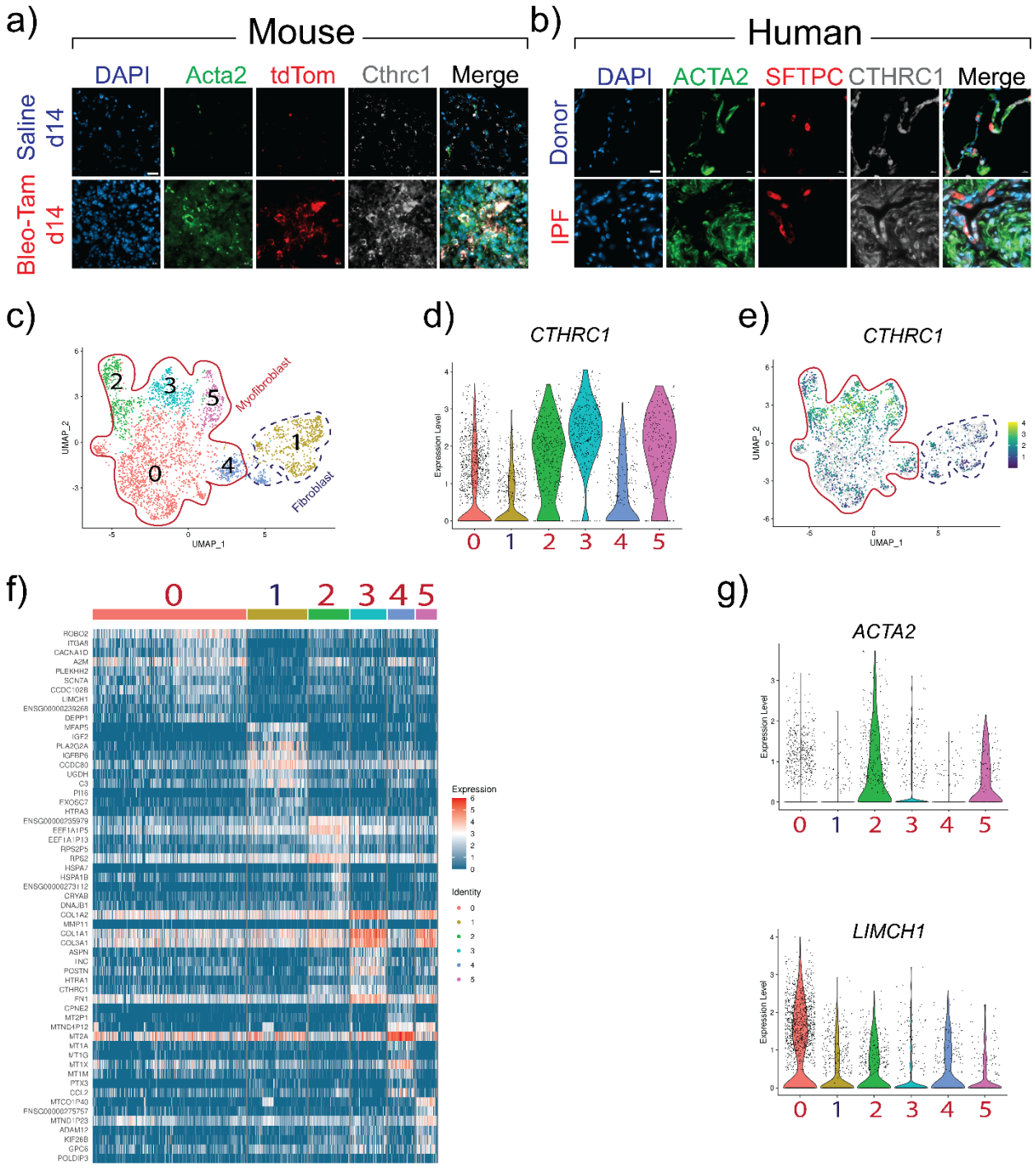
a)
Mouse
DAPI
Acta2
tdTom
Cthrc1
Merge
Saline d14
Bleo-Tam d14
b)
Human
DAPI
ACTA2
SFTPC
CTHRC1
Merge
Donor
IPF
c)
Myofibroblast
Fibroblast
UMAP_1
UMAP_2
d)
CTHRC1
Expression Level
e)
CTHRC1
f)
Expression
Identity
g)
ACTA2
LIMCH1
Expression Level

Figure 7: **Human IPF lungs display heterogeneity in the CTHRC1 population.**

a) Immunofluorescence for Acta2, Rfp (tdTom^{pos}) and Cthrc1 in saline and Bleo-Tam lungs at day 14. Note the low expression of Cthrc1 in the saline and the substantial increase in Cthrc1 expression in the fibrotic regions of the Bleo-Tam lungs. Note the overlap between tdTom^{pos} cells and Cthrc1. **b)** Immunofluorescence for ACTA2, SFTPC and CTHRC1 in donor and IPF lungs. CTHRC1 is detected at a low level in SFTPC^{pos} cells in the donor. Note the accumulation of CTHRC1/ACTA2^{pos} myofibroblasts in the IPF lungs. **c)** UMAP of selected *CTHRC1^{pos}* fibroblast clusters from IPF lungs. The two initial fibroblast and myofibroblast populations were further subclustered into 6 clusters. **d)** Corresponding violin plots for *CTHRC1* expression. Note that the MyoFib. Subclusters (2, 3 and 5) display the highest levels of *CTHRC1* expression. **e)** Feature map of *CTHRC1* expression in different clusters. **f)** Corresponding heatmap showing the top 10 markers for each cluster. Please note that Cluster 0 belongs to MyoFib. expresses LIF markers such as *LIMCH1* and *ROBO2*. Cluster 3 expressed a high level of fibrotic markers such as *COL1A1, TNC, COL3A1, POSTN* and *FN1.* **g)** Violin plots for *ACTA2* and *LIMCH1*. Note that *LIMCH1* is detected in all the subclusters with an abundant expression in cluster 0. Scale bar: a and b:20µm

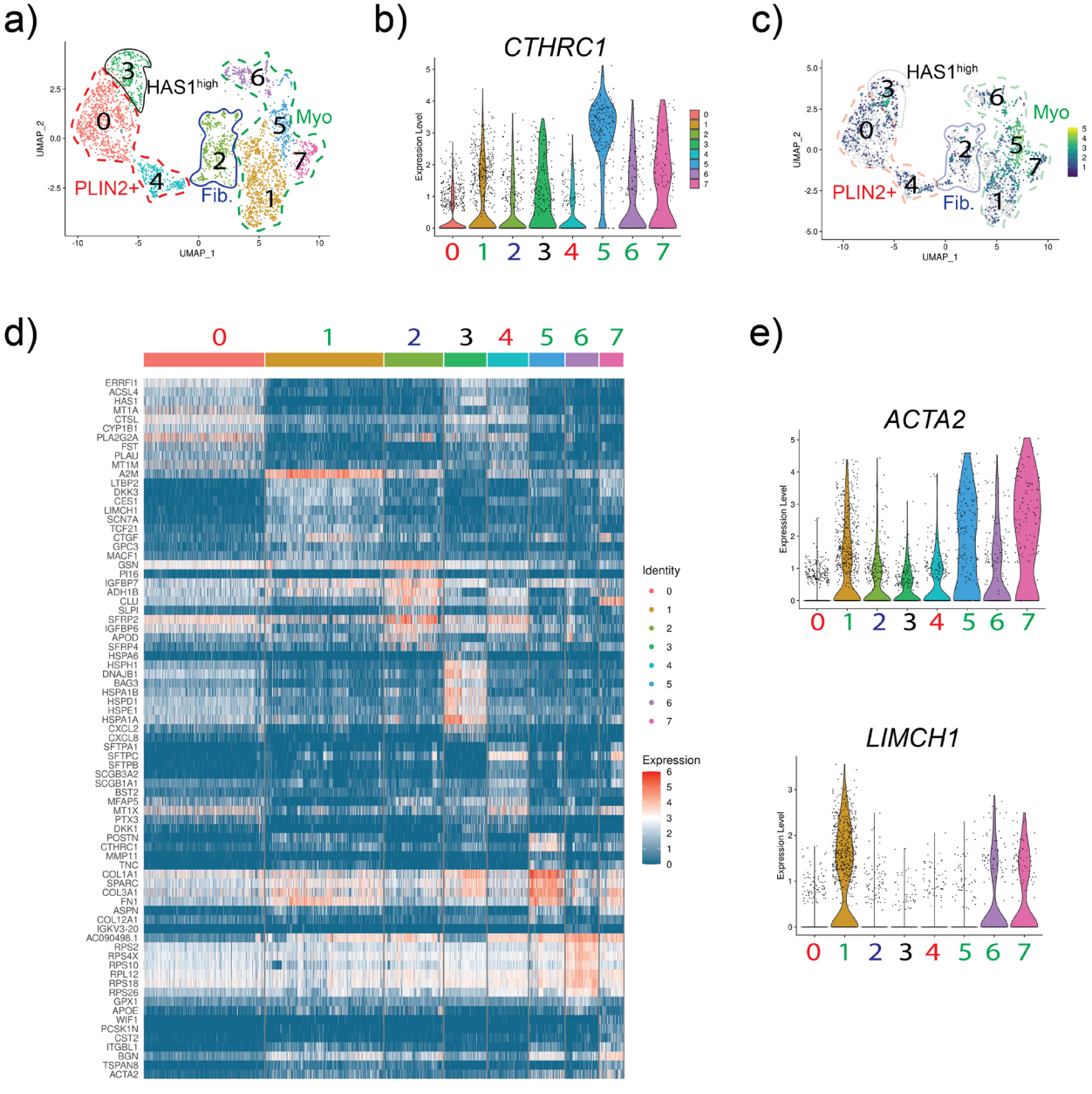
a)
HAS1high
Myo
PLIN2+
Fib.
UMAP_1
UMAP_2
b)
CTHRC1
Expression Level
0 1 2 3 4 5 6 7
c)
HAS1high
Myo
PLIN2+
Fib.
UMAP_1
UMAP_2
d)
0 1 2 3 4 5 6 7
ERRFI1
ACSL4
HAS1
MT1A
CTSL
CYP1B1
PLA2G2A
FST
PLAU
MT1M
A2M
LTBP2
DKK3
CES1
LIMCH1
SCN7A
TCF21
CTGF
GPC3
MACF1
GSN
PI16
IGFBP7
ADH1B
CLU
SLPI
SFRP2
IGFBP6
APOD
SFRP4
HSPA6
HSPH1
DNAJB1
BAG3
HSPA1B
HSPD1
HSPE1
HSPA1A
CXCL2
CXCL8
SFTPA1
SFTPC
SFTPB
SCGB3A2
SCGB1A1
BST2
MFAP5
MT1X
PTX3
DKK1
POSTN
CTHRC1
MMP11
TNC
COL1A1
SPARC
COL3A1
FN1
ASPN
COL12A1
IGKV3-20
AC090498.1
RPS2
RPS4X
RPS10
RPL12
RPS18
RPS26
GPX1
APOE
WIF1
PCSK1N
CST2
ITGBL1
BGN
TSPAN8
ACTA2
Identity
0 1 2 3 4 5 6 7
Expression
e)
ACTA2
Expression Level
0 1 2 3 4 5 6 7
LIMCH1
Expression Level
0 1 2 3 4 5 6 7

Figure 8: **Heterogeneity of CTHRC1 population Human IPF lungs.**

a) UMAP of selected *CTHRC1*^{pos} fibroblast populations from IPF lungs. The 4 initial fibroblast populations (HAS1^{high} fib., PLIN2+ Fib., Fib., MyoFib.) were further subclustered into 8 clusters. **b)** Corresponding violin plots for *CTHRC1* expression. Note that the MyoFib. Subclusters (1, 5, 6 and 7) are displaying the highest levels of *CTHRC1* expression. **c)** *CTHRC1* expression in the UMAP. **d)** Corresponding heatmap showing the top 10 markers for each cluster. Please note that Cluster 1 belongs to MyoFib. expresses LIF markers such as *LIMCH1*, *TCF21*, *MACF1* and *APOE*. Cluster 5 expressed a high level of fibrotic markers such as *COL1A1*, *SPARC*, *COL3A1* and *FN1*. **e)** Violin plots for *ACTA2* and *LIMCH1*. Note that *ACTA2* is detected in all the subclusters with a minimal expression in cluster 0. *LIMCH1* is detected in the MyoFb. clusters suggesting a LIF to MYF transition.

4.5 Characterization of the fate of the *Cthrc1*^{pos} subclusters during fibrosis resolution in Bleo-Tam mice

To investigate the fate of the different *Acta2*^{pos} mesenchymal populations during fibrosis resolution, we also captured tdTom^{pos} cells by flow cytometry at day 60 following Bleo administration (Bleo-Tam condition). Isolated cells were subjected to scRNA-seq and compared to *Acta2*^{pos} cells from Bleo-Tam lungs collected on day 14. We obtained a total of 5,059 cells recovered after quality control (Figure 4a and b).

Figure 9a displays the UMAP plot corresponding to the integrated data. It became apparent that a strong decrease in the abundance of *Cthrc1*^{pos} myofibroblasts pool had occurred. The distribution of the different clusters in Bleo-Tam lungs at day 14 and 60 confirmed that the *Cthrc1*^{pos} myofibroblasts are drastically reduced at day 60 with Ct3, and Ct4 was barely detected at day 60 (Figure 9a, b). Interestingly, the percentile of alveolar fibroblasts was moderately increased at day 60 compared to day 14 while that of peribronchial fibroblasts was strongly increased (Figure 9c). The violin plot for *Cthrc1* expression indicated that subclusters Ct1 and Ct2 display a strong reduction in *Cthrc1* expression at day 60 (Figure 9d).

Next, we focused on the *Cthrc1*^{pos} subclusters. Figure 9e shows the UMAP plot for the *Cthrc1*^{pos} subclusters from integrated datasets of Bleo-Tam lungs at days 14 and 60. Ct1 and Ct2 are the most abundant, representing 31.1% and 35.4% of the overall *Cthrc1*^{pos} cells. As previously described (Figure 9a, c), *Cthrc1*^{pos} cells from each subcluster were massively decreased in the context of fibrosis resolution. A close examination of the heatmap showing the main differentially expressed genes for each *Cthrc1* subcluster (Figure 9f) revealed that Ct1 reinforced its transcriptomic signature at day 60. Notably, Ct2 acquired a partial Ct1 signature during fibrosis resolution. Unfortunately, the resolution for Ct3 and Ct4 could not be carried out as these cells were minimally detected at day 60.

The fate of alveolar fibroblasts during fibrosis resolution was also analyzed. The UMAP plot of alveolar fibroblast subclusters from integrated datasets of Bleo-Tam lungs at days 14 and 60 are shown in figure 9h. Al3 is the most abundant one representing 56.5% of total alveolar fibroblasts. Interestingly, a drop of fibrotic markers *Sfrp1*, *Col3a1*, *Col1a1,*

and *Col5a2* was detected in this subcluster during fibrosis resolution. At the same time, a much stronger LIF-like signature was observed in Al2, likely illustrating a return to a reinforced LIF phenotype (Figure 9i). Indeed, the expression of the LIF signature showed enrichment in both Ct1 and Al2 during fibrosis resolution. (Figure 9k).

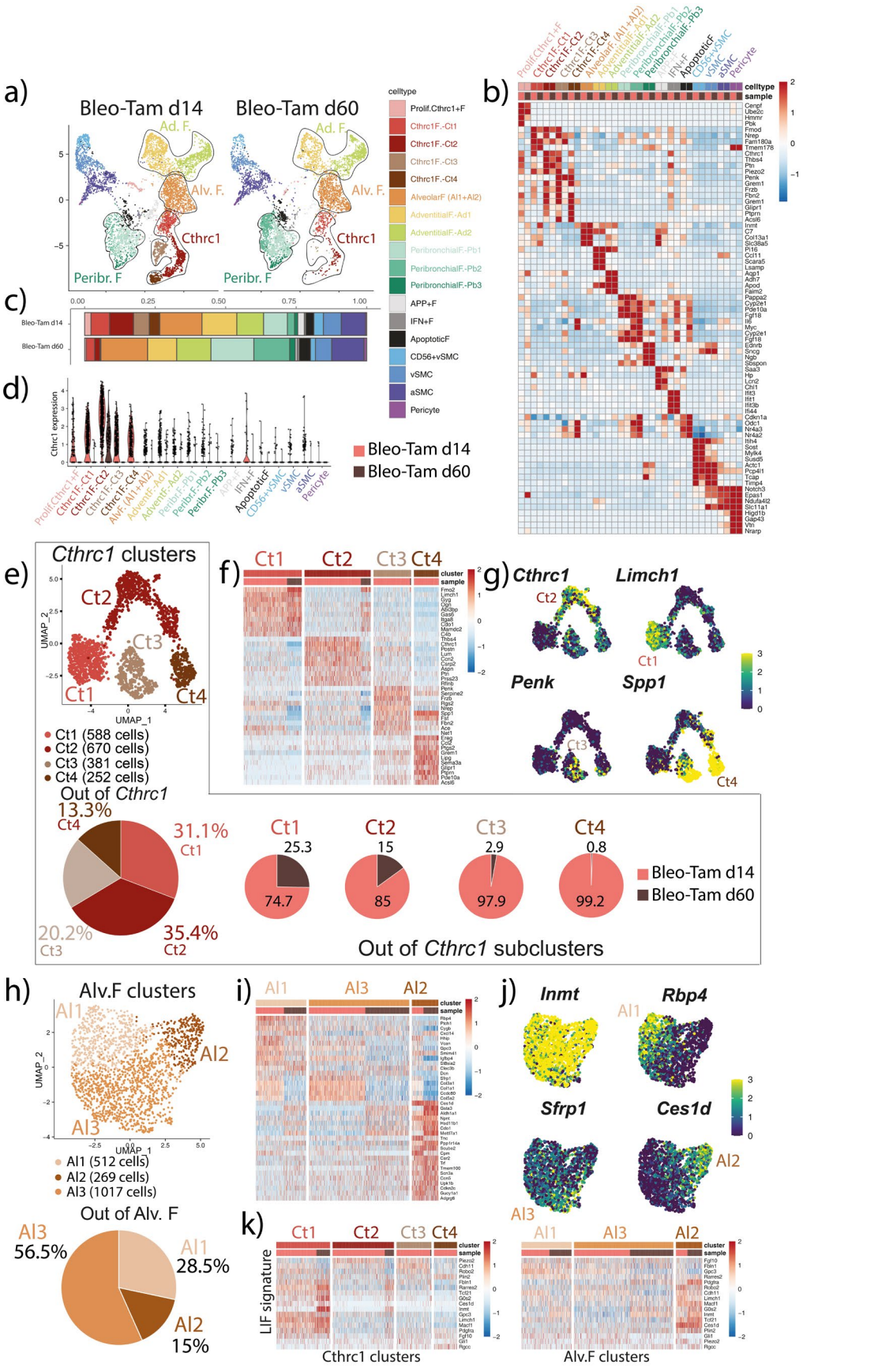
a)
Bleo-Tam d14
Bleo-Tam d60
Ad. F.
Alv. F.
Cthrc1
Peribr. F
celltype
Prolif.Cthrc1+F
Cthrc1F.-Ct1
Cthrc1F.-Ct2
Cthrc1F.-Ct3
Cthrc1F.-Ct4
AlveolarF (Al1+Al2)
AdventitialF.-Ad1
AdventitialF.-Ad2
PeribronchialF.-Pb1
PeribronchialF.-Pb2
PeribronchialF.-Pb3
APP+F
IFN+F
ApoptoticF
CD56+vSMC
vSMC
aSMC
Pericyte
b)
celltype
sample
c)
Bleo-Tam d14
Bleo-Tam d60
d)
Cthrc1 expression
Bleo-Tam d14
Bleo-Tam d60
e)
Cthrc1 clusters
UMAP_1
UMAP_2
Ct1 (588 cells)
Ct2 (670 cells)
Ct3 (381 cells)
Ct4 (252 cells)
Out of Cthrc1
13.3%
Ct4
31.1%
Ct1
20.2%
Ct3
35.4%
Ct2
f)
Ct1
Ct2
Ct3
Ct4
g)
Cthrc1
Limch1
Penk
Spp1
Ct1
Ct2
Ct3
Ct4
Ct1
25.3
74.7
Ct2
15
85
Ct3
2.9
97.9
Ct4
0.8
99.2
Bleo-Tam d14
Bleo-Tam d60
Out of Cthrc1 subclusters
h)
Alv.F clusters
Al1
Al2
Al3
Al1 (512 cells)
Al2 (269 cells)
Al3 (1017 cells)
Out of Alv. F
Al3
56.5%
Al1
28.5%
Al2
15%
i)
Al1
Al3
Al2
j)
Inmt
Rbp4
Sfrp1
Ces1d
Al1
Al2
Al3
k)
Ct1
Ct2
Ct3
Ct4
LIF signature
Cthrc1 clusters
Al1
Al3
Al2
Alv.F clusters

Figure 9: **Characterization of the fate of the *Cthrc1*^{pos} subclusters during fibrosis resolution.**

a) Integrated UMAP of *Acta2*^{pos} cells isolated from Bleo-Tam lungs at day 14 and 60 post-bleo injury showing a strong decrease in the *Cthrc1*^{pos} myofibroblasts. **b)** Heatmap showing genes enriched for each cluster. **c)** Distribution of the different clusters in Bleo-Tam lungs at day 14 and 60. Note that the *Cthrc1*^{pos} myofibroblasts are drastically reduced at day 60. Ct3 and Ct4 clusters are barely detected at day 60. The percentile of alveolar fibroblasts is modestly increased while the peribronchial fibroblasts populations are strongly increased. **d)** Violin plot for *Cthrc1* expression. Clusters Ct1 and Ct2 display a strong reduction in *Cthrc1* expression at day 60. **e)** Integrated UMAP of the Cthrc1 clusters from Bleo-Tam lungs at day 14 and 60. Ct2 represents 35.4% of the overall *Cthrc1*^{pos} cells. Cthrc1^{pos} cells from each subcluster are massively decreased in the context of fibrosis resolution. **f)** Heatmap showing the main differentially expressed genes for each *Cthrc1*^{pos} subclusters. Note that Ct1 re-enforces its transcriptomic signature at day 60. Importantly, Ct2 reacquires the Ct1 signature during fibrosis resolution. Resolution cannot be analyzed for Ct3 and Ct4 as these cells are minimally detected at day 60. **g)** Expression of *Cthrc1*, *Limch1*, *Penk* and *Spp1* on feature plots. **h)** Integrated UMAP of the alveolar fibroblasts subclusters from Bleo-Tam lungs at day 14 and 60. Note that the newly formed Al3 represents 56.5% of the total alveolar fibroblasts cluster. **i)** Heatmap showing the main differentially expressed genes for each alveolar fibroblasts subclusters. Note that Al3 drops its fibrotic markers *Sfrp1*, *Col3a1*, *Col1a1* and *Col5a2*. **j)** Expression of LIF marker *Inmt*, the differentially expressed gene *Rbp4*, the fibrotic gene *Sfrp1* and the LIF marker *Ces1d* on feature plots. **k)** Expression of the LIF signature in the different *Cthrc1*^{pos} subclusters indicates enrichment in Ct1 during fibrosis resolution. This signature is also enriched in Al2 of the alveolar fibroblasts.

4.6 Characterization of the fate of the *Cthrc1^{pos}* clusters during fibrosis resolution in Tam-Bleo mice

Next, we investigated the fate of the pre-existing Acta2^{pos} LIF and Acta2^{pos} Cthrc1, labeled in Tam-Bleo, during fibrosis resolution. In particular, whether the LIFs appearing during resolution also arise from pre-existing LIFs that never became aMYFs.

We captured tdTom^{pos} cells by flow cytometry at day 60 following Bleo administration (Tam-Bleo condition). Isolated cells were subjected to scRNA-seq and compared to *Acta2^{pos}* cells from Tam-Bleo lungs collected on day 14. We obtained a total of 11316 cells recovered after quality control (Figure 4a and b).

Our results displayed in the integrated UMAP indicate that *Cthrc1^{pos}* aMYF arising from *Acta2^{pos}* cells labeled before Bleo injury are mostly cleared during resolution (Figure 10a). The distribution of the different clusters in Tam-Bleo day 14 and day 60 supports the decrease in the *Cthrc1^{pos}* myofibroblasts at day 60. Interestingly, the alveolar fibroblasts and adventitial fibroblasts are abundantly increased at day 60 while a reduction of the peribronchial fibroblast clusters, especially Pb1, is observed (Figure 10c).

The corresponding UMAP of the *Cthrc1* clusters indicates that Ct2 represents 50.2% of the overall *Cthrc1^{pos}* cells. The Ct4 is completely cleared at day 60 (Figure 10e).

The heatmap showing the main differentially expressed genes for each *Cthrc1* subclusters indicates that Ct1 re-enforces its transcriptomic signature at day 60, while Ct2 reacquires the Ct1 signature during fibrosis resolution at day60 (Figure 10f).

Finally, the UMAP of the alveolar fibroblasts subclusters from Tam-Bleo day 14 and day 60 indicates that Al1 represents 89.4% of the total alveolar fibroblasts (Figure 10h). In addition, the heatmap showing the main differentially expressed genes for each alveolar fibroblasts subclusters indicates that these genes are not impacted by resolution (Figure 10i).

Expression of the LIF signature in the different *Cthrc1* subclusters indicates enrichment in Ct1 during fibrosis resolution. This signature is also enriched in Al2 of the alveolar fibroblasts (Figure 10k). Interestingly, a close-up comparison of the Al2 at day 60 vs. d14

does not indicate enrichment in the LIF signature during resolution suggesting that Acta2^{pos} pre-existing LIFs did not display a fully differentiated LIF phenotype.

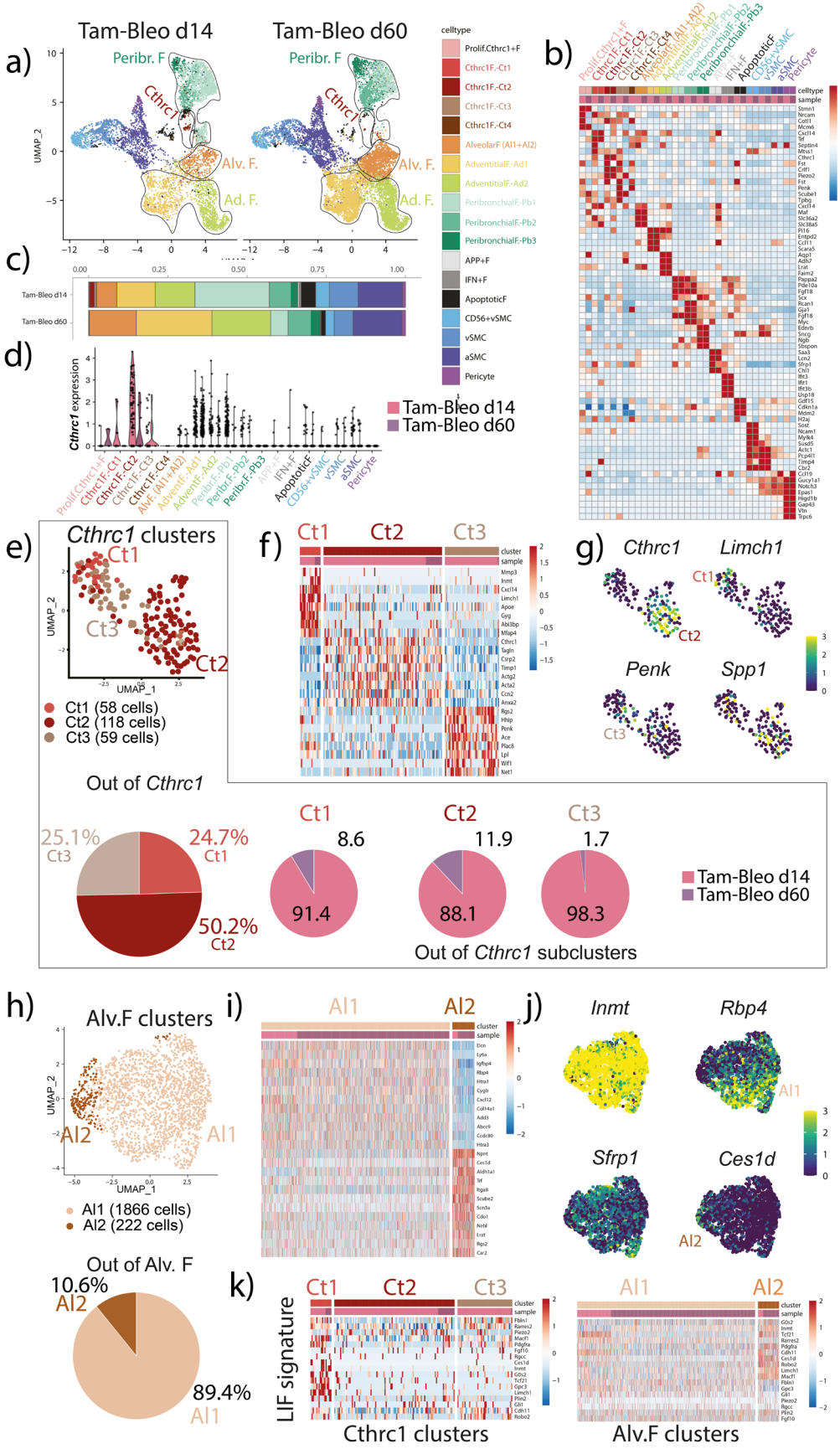
a)
Tam-Bleo d14
Tam-Bleo d60
Peribr. F
Cthrc1
Alv. F.
Ad. F.
UMAP_2
UMAP_1
celltype
Prolif.Cthrc1+F
Cthrc1F.-Ct1
Cthrc1F.-Ct2
Cthrc1F.-Ct3
Cthrc1F.-Ct4
AlveolarF (Al1+Al2)
AdventitialF-Ad1
AdventitialF-Ad2
PeribronchialF-Pb1
PeribronchialF-Pb2
PeribronchialF-Pb3
APP+F
IFN+F
ApoptoticF
CD56+vSMC
vSMC
aSMC
Pericyte
b)
c)
Tam-Bleo d14
Tam-Bleo d60
d)
Cthrc1 expression
Tam-Bleo d14
Tam-Bleo d60
e)
Cthrc1 clusters
Ct1
Ct2
Ct3
Ct1 (58 cells)
Ct2 (118 cells)
Ct3 (59 cells)
f)
Ct1
Ct2
Ct3
cluster
sample
g)
Cthrc1
Limch1
Penk
Spp1
Out of Cthrc1
25.1%
Ct3
24.7%
Ct1
50.2%
Ct2
Ct1
8.6
91.4
Ct2
11.9
88.1
Ct3
1.7
98.3
Tam-Bleo d14
Tam-Bleo d60
Out of Cthrc1 subclusters
h)
Alv.F clusters
Al2
Al1
Al1 (1866 cells)
Al2 (222 cells)
Out of Alv. F
10.6%
Al2
89.4%
Al1
i)
Al1
Al2
j)
Inmt
Rbp4
Sfrp1
Ces1d
k)
LIF signature
Ct1
Ct2
Ct3
Cthrc1 clusters
Al1
Al2
Alv.F clusters

Figure 10: ***Acta2^{pos}*** **cells labeled before bleomycin injury are mostly cleared from** ***Cthrc1^{pos}*** **myofibroblast clusters during resolution.**

a) Integrated UMAP of *Acta2^{pos}* cells isolated from Tam-Bleo lungs at day 14 and day 60 post-bleo injury showing 18 distinct clusters including alveolar fibroblasts, peribronchial fibroblasts, adventitial fibroblasts and Cthrc1^{pos} myofibroblasts. **b)** Heatmap showing genes enriched for each cluster. **c)** Distribution of the different clusters in Tam-Bleo day 14 and day 60. Note that the decrease in the Cthrc1^{pos} myofibroblasts at day 60. The alveolar fibroblasts, adventitial fibroblasts are abundantly increased at day 60 while a minor decrease in the peribronchial fibroblasts clusters. **d)** Violin plot for *Cthrc1* expression indicates that the Ct2 cluster displays the highest expression level. **e)** Integrated UMAP of the Cthrc1 clusters from Tam-Bleo day 14 and day 60 lungs. Ct2 represents 50.2% of the overall *Cthrc1^{pos}* cells. Note that the Ct4 cluster is completely cleared at day 60. **f)** Heatmap showing the main differentially expressed genes for each *Cthrc1* subclusters. Note that Ct1 re-enforces its transcriptomic signature at day 60. Interestingly, Ct2 reacquires the Ct1 signature during fibrosis resolution could be visualized with minimal cells detected at day 60. **g)** Expression of *Cthrc1*, *Limch1*, *Penk* and *Spp1* on feature plots. **h)** Integrated UMAP of the alveolar fibroblasts subclusters from from Tam-Bleo day 14 and day 60. Note that Al1 represents 56.5% of the total alveolar fibroblasts. **i)** Heatmap showing the main differentially expressed genes for each alveolar fibroblasts subclusters. **j)** Expression of alveolar fibroblasts marker *Inmt*, the differentially expressed gene *Rbp4*, the fibrotic gene *Sfrp1* and the differentially expressed gene *Ces1d* on feature plots. **k)** Expression of the LIF signature in the different *Cthrc1* subclusters indicates enrichment in Ct1 during fibrosis resolution. This signature is also enriched in Al2 of the alveolar fibroblasts.

4.7 The peribronchial fibroblasts and adventitial fibroblasts are also impacted during fibrosis formation and resolution.

The peribronchial and adventitial fibroblasts represent 40% of the total *Acta2*^{pos} cells labeled in the lung, and as such, they also represent a potential target population that Bleo could impact. Therefore, we analyzed these two populations in saline, Tam-Bleo, and Bleo-Tam on days 14 and 60 (Figures 11 and 12).

Subclustering of the peribronchial fibroblasts indicates the presence of 3 subclusters (Pb1-3) (Figure 11). Upon Bleo injury, irrespective of the labeling before or during injury, cells in Pb1 and Pb2 upregulate fibrotic genes like *Eln*, *Ltbp2,* and *Sfrp1* (Figure 11b, f, j, and n). At day 60 (during resolution), we observed a decrease in the expression of these fibrotic markers in these subclusters. The expression of the LIF signature in the different peribronchial subclusters is homogenously low throughout the different subclusters and is not impacted during fibrosis formation and resolution. These results suggest that the peribronchial fibroblasts and the LIFs are two distinct lineages. Ct3 expresses *Lgr6* (Figure 5f) and *Hhip* (Figure 10f) during fibrosis formation. These results suggest that Pb1 and Pb2 could contribute to Ct3 cells.

Subclustering of the adventitial fibroblasts indicated the presence of 2 subclusters (Ad1 and 2) (Figure 12). Regardless of the labeling before or during injury, the gene signature for these two clusters does not appear to be significantly impacted during fibrosis formation and resolution. Ad2 expresses a higher LIF signature level than Ad1, and the LIF signature seems to be downregulated by Bleo treatment (Figure 12d). When cells are labeled before injury (Tam-Bleo), the LIF signature in Ad2 is enhanced during resolution with an increase for *Inmt*, *Limch1,* and *Macf1* (Figure 12l). In contrast, when cells are labeled during injury (Bleo-Tam), cells in Ad2 decrease the expression of *Cdh11*, *Robo2,* and *Limch1* (Figure 12p). We, therefore, conclude that adventitial and LIFs likely share common characteristics and signatures. One exciting possibility is that adventitial fibroblasts acquiring LIF characteristics could compensate for the loss of LIFs due to their transition towards the *Cthrc1*^{pos} aMYF phenotype.

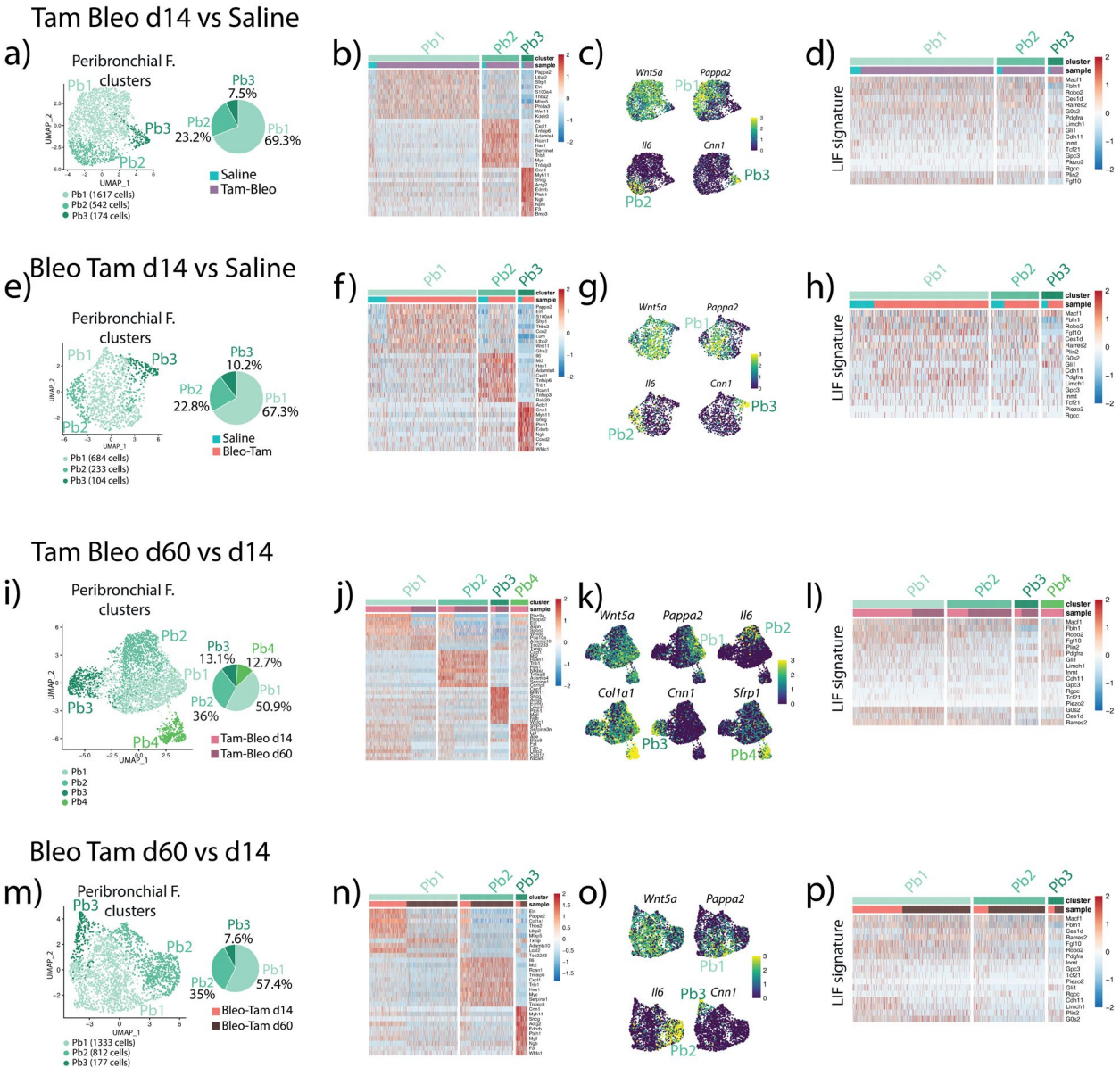
Tam Bleo d14 vs Saline
a)
Peribronchial F. clusters
Pb1
Pb2
Pb3
UMAP_1
UMAP_2
Pb3 7.5%
Pb2 23.2%
Pb1 69.3%
Saline
Tam-Bleo
Pb1 (1617 cells)
Pb2 (542 cells)
Pb3 (174 cells)
b)
c)
Wnt5a
Pappa2
Il6
Cnn1
d)
LIF signature
Bleo Tam d14 vs Saline
e)
Peribronchial F. clusters
Pb3 10.2%
Pb2 22.8%
Pb1 67.3%
Saline
Bleo-Tam
Pb1 (684 cells)
Pb2 (233 cells)
Pb3 (104 cells)
f)
g)
h)
Tam Bleo d60 vs d14
i)
Peribronchial F. clusters
Pb4
Pb3 13.1%
Pb4 12.7%
Pb1 50.9%
Pb2 36%
Tam-Bleo d14
Tam-Bleo d60
Pb1
Pb2
Pb3
Pb4
j)
k)
Col1a1
Sfrp1
l)
Bleo Tam d60 vs d14
m)
Peribronchial F. clusters
Pb3 7.6%
Pb1 57.4%
Pb2 35%
Bleo-Tam d14
Bleo-Tam d60
Pb1 (1333 cells)
Pb2 (812 cells)
Pb3 (177 cells)
n)
o)
p)

Figure 11: **Subclustering of peribronchial fibroblasts in saline, Tam-Bleo, and Bleo-Tam lungs at day 14 and day 60 post-bleo injury.**

a) Integrated UMAP of peribronchial fibroblasts isolated from saline and Tam-Bleo lungs at day 14 post-bleo injury showing 3 distinct clusters. Note that Pb1 represents 69.3% of the total peribronchial F. **b)** Heatmap showing genes enriched for each cluster. Note that upon bleo injury, Pb1 and 2 upregulate fibrotic genes like *Eln*, *Ltbp2* and *Sfrp1.* Note also that Pb1 displays a downregulation of its saline signature in bleo. This is not observed for Pb2 and 3. **c)** Expression of the general peribronchial fibroblast marker *Wnt5a*. Expression also of genes specific of Pb1 (*Pappa2*), Pb2 (*Il6*), and Pb3 (*Cnn1*) on feature plots. **d)** Expression of the LIF signature in the different peribronchial subclusters showing homogenous lower expression throughout the different clusters. **e)** Integrated UMAP of peribronchial fibroblasts isolated from saline and Bleo-Tam lungs at day 14 post-bleo injury showing 3 distinct clusters. Note that Pb1 represents 67.3% of the total peribronchial F. **f)** Heatmap showing genes enriched for each cluster. Similar observations to the ones described in b) were made. **g)** Expression of *Wnt5a*, *Pappa2*, *Il6* and *Cnn1* on feature plots. **h)** Expression of the LIF signature in the different peribronchial subclusters. **i)** Integrated UMAP of peribronchial fibroblasts isolated from Tam-Bleo lungs at day 60 and day 14 post-bleo injury showing 4 distinct clusters. Pb1 represents 50.9% of the total Peribronchial F. **j)** Heatmap showing genes enriched for each cluster. Note the decrease in the expression of the fibrotic markers *Eln* and *Sfrp1* in Pb1 and 2 during resolution at day 60. Pb3 and 4 (please note that Pb4 is seen only in the integrated analysis of Tam-Bleo day14 and Tam-Bleo day d60. In contrast, when all datasets of this study were integrated and analyzed, Pb4 is absent. This is due to the sample-to-sample variation corrections made for the integration) are not impacted by resolution. **k)** Expression of *Wnt5a*, *Pappa2*, *Il6*, *Col1a1*, *Cnn1* and *Sfrp1* on feature plots. **l)** Expression of the LIF signature in the different peribronchial subclusters. **m)** Integrated UMAP of peribronchial fibroblasts isolated from Bleo-Tam lungs at day 60 and day 14 post-bleo injury showing 3 distinct clusters. Pb1 represents 57.4% of the total peribronchial F. **n)** Heatmap showing genes enriched for each cluster. Note the loss of fibrotic markers in Pb1 and 2 during resolution at day 60. Pb3 is not impacted by resolution. **o)** Expression of *Wnt5a*, *Pappa2*, *Il6* and *Cnn1* on feature plots. **p)** Expression of the LIF signature in the different peribronchial subclusters.

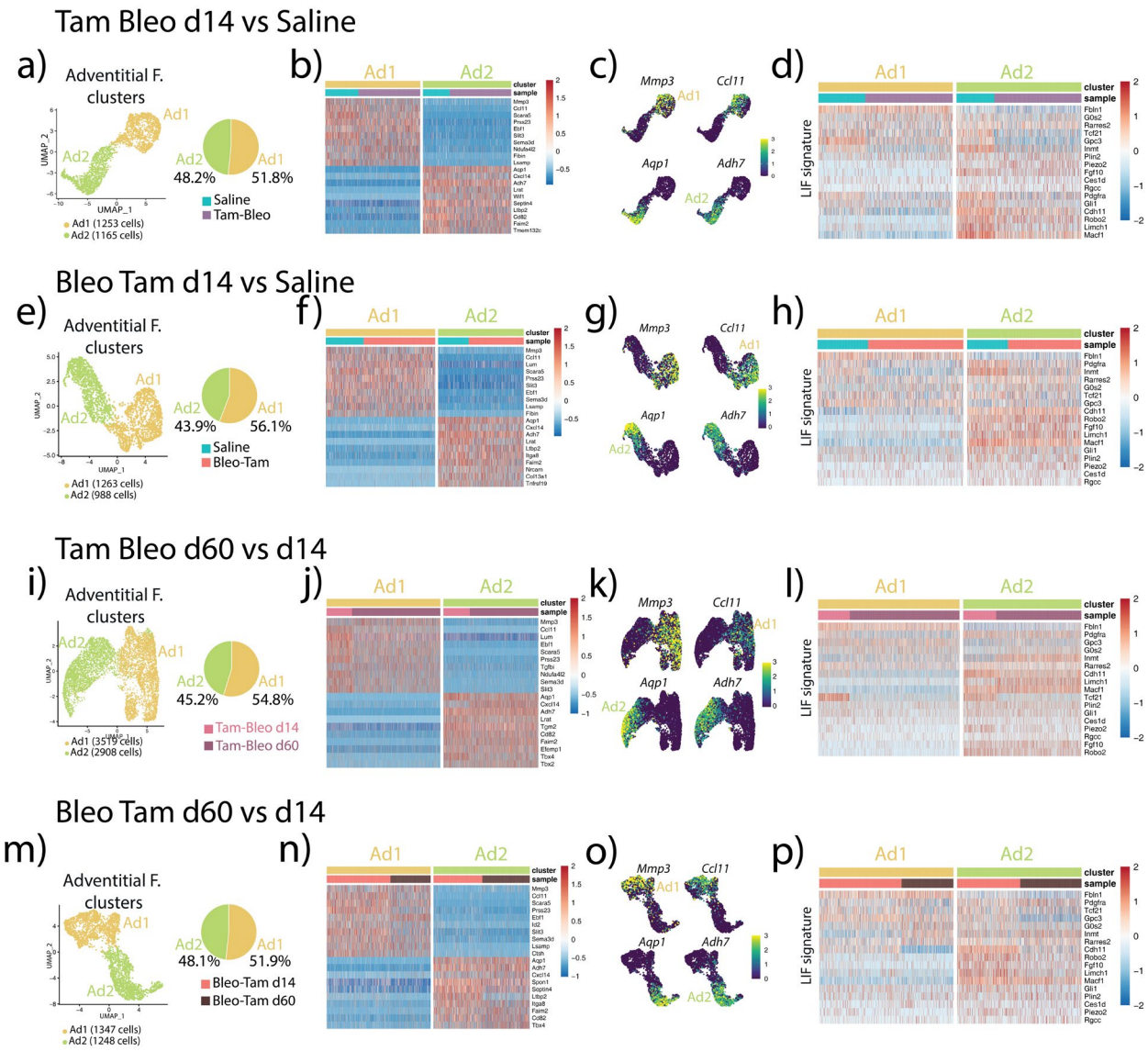
Tam Bleo d14 vs Saline
a)
Adventitial F. clusters
Ad1
Ad2
UMAP_1
UMAP_2
Ad1 (1253 cells)
Ad2 (1165 cells)
48.2%
51.8%
Saline
Tam-Bleo
b)
Ad1
Ad2
cluster
sample
c)
Mmp3
Ccl11
Aqp1
Adh7
d)
LIF signature
Bleo Tam d14 vs Saline
e)
Adventitial F. clusters
Ad1 (1263 cells)
Ad2 (988 cells)
43.9%
56.1%
Saline
Bleo-Tam
f)
g)
h)
Tam Bleo d60 vs d14
i)
Adventitial F. clusters
Ad1 (3519 cells)
Ad2 (2908 cells)
45.2%
54.8%
Tam-Bleo d14
Tam-Bleo d60
j)
k)
l)
Bleo Tam d60 vs d14
m)
Adventitial F. clusters
Ad1 (1347 cells)
Ad2 (1248 cells)
48.1%
51.9%
Bleo-Tam d14
Bleo-Tam d60
n)
o)
p)

Figure 12: **Subclustering of adventitial fibroblasts in saline, Tam-Bleo, and Bleo-Tam lungs at day 14 and 60 post-bleo injury. a)** Integrated UMAP of adventitial fibroblasts isolated from saline and Tam-Bleo lungs at day 14 showing 2 distinct clusters (Ad1 and Ad2). These clusters are almost equally represented within the adventitial fibroblasts population. **b)** Heatmap showing genes enriched for each cluster. Note that the gene signature for each cluster is not significantly impacted by bleomycin treatment. **c)** Expression of genes specific of Ad1 (*Mmp3* and *Ccl11*) and Ad2 (*Aqp1* and *Adh7*) on feature plots. **d)** Expression of the LIF signature. Note that Ad2 in saline expresses a higher level of the LIF signature. This signature is reduced upon bleomycin treatment. **e)** Integrated UMAP of adventitial fibroblasts isolated from saline and Bleo-Tam lungs at day 14 showing 2 distinct clusters (Ad1 and Ad2). Ad1 represents 56.1% of the total adventitial fibroblasts population. **f)** Heatmap showing genes enriched for each cluster. Note that the gene signature for each cluster is not significantly impacted by bleomycin treatment. **g)** Expression of *Mmp3*, *Ccl11*, *Aqp1* and *Adh7* on feature plots. **h)** Expression of the LIF signature. Note that Ad2 in saline expresses a higher level of the LIF signature. This signature is not impacted upon bleomycin treatment. Acta2^{neg} cells acquiring *Acta2* expression and belonging to this cluster display part of the LIF signature. **i)** Integrated UMAP of adventitial fibroblasts isolated from Tam-Bleo lungs at day 60 and day 14. Ad1 represents 54.8% of the total adventitial fibroblasts population. **j)** Heatmap showing genes enriched for each cluster. Note that the gene signature for each cluster is not significantly impacted during fibrosis resolution. **k)** Expression of *Mmp3*, *Ccl11*, *Aqp1* and *Adh7* on feature plots. **l)** Expression of the LIF signature. Note that Ad2 Tam-Bleo d60 expresses a slightly higher level of the LIF signature compared to day 14. Ad1 displays also a downregulation of *Tcf21* during resolution. (Such downregulation in *Tcf21* is also seen in Ad2 in Bleo-Tam day 60 vs day 14). **m)** Integrated UMAP of adventitial fibroblasts isolated from Bleo-Tam lungs at day 60 and day 14. The 2 clusters are again almost equally represented within the adventitial fibroblasts population. **n)** Heatmap showing genes enriched for each cluster. Note that the gene signature for each cluster is not significantly impacted by bleomycin treatment. **o)** Expression of *Mmp3*, *Ccl11*, *Aqp1* and *Adh7* on feature plots. **p)** Expression of the LIF signature. Note that Ad2 Bleo-Tam d14 expresses a higher level of the LIF signature. This signature is partially reduced at day 60 (for the expression of *Cdh11*, *Robo2*, *Fgf10* and *Limch1*).

4.8 Evaluation of the resident mesenchymal cell niche activity for AT2 stem cells during fibrosis formation and resolution.

Next, we evaluated the status of the niche activity displayed by rMCs during fibrosis formation and resolution (Figure 13a). Suggesting that resolution was not complete at day 60; we could still detect using H&E (Figure 13c) and IF (Figure 13b), some fibrotic areas containing tdTom^{pos} cells. We focused on the Sca1^{pos} rMC pool, which has been reported to be enriched in LIFs and includes the niche activity for AT2 cells (Taghizadeh et al., 2022; Taghizadeh et al., 2021).

The gating strategy to sort CD31/CD45/EpCAM triple-negative rMCs positive for Sca1 (Sca1^{pos} rMCs) in saline, Tam-Bleo day 14, Tam-Bleo day 30, and Tam-Bleo day 60 lungs, as well as AT2s from C57BL/6 mice lungs (CD31neg CD45neg Epcam^{pos} Lysotracker^{pos}), is shown in Figure 13d. Isolated AT2 and Sca1^{pos} rMC cells were then co-cultured in Matrigel for 14 days (alveolosphere assay), and organoid formation was visualized using bright field microscopy (Figure 13e). Interestingly, the rMC niche activity is significantly reduced at the peak of fibrosis (Tam-Bleo day 14) and completely lost during fibrosis resolution (Tam-Bleo day 30 and Tam-Bleo day 60). The quantification of colony-forming efficiency (CFE) confirms the decrease in rMC stem cell niche activity during fibrosis formation and the lack of recovery during fibrosis resolution (Figure 13f).

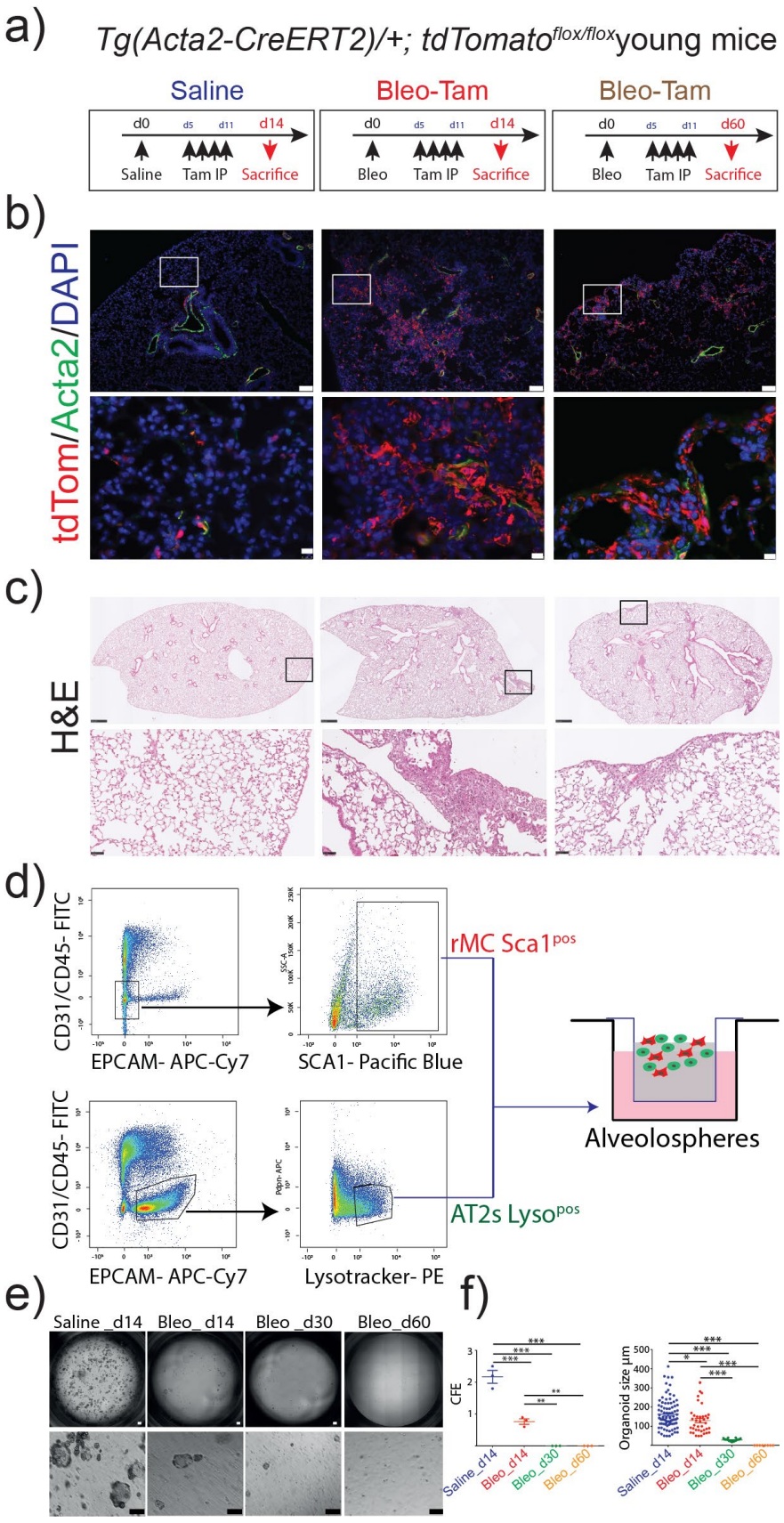
a)
Tg(Acta2-CreERT2)/+; tdTomato flox/flox young mice
Saline
Bleo-Tam
Bleo-Tam
d0 d5 d11 d14
Saline Tam IP Sacrifice
d0 d5 d11 d14
Bleo Tam IP Sacrifice
d0 d5 d11 d60
Bleo Tam IP Sacrifice
b)
tdTom/Acta2/DAPI
c)
H&E
d)
CD31/CD45- FITC
EPCAM- APC-Cy7
SCA1- Pacific Blue
rMC Sca1pos
CD31/CD45- FITC
EPCAM- APC-Cy7
Lysotracker- PE
AT2s Lysopos
Alveolospheres
e)
Saline_d14
Bleo_d14
Bleo_d30
Bleo_d60
f)
CFE
Organoid size µm
Saline_d14
Bleo_d14
Bleo_d30
Bleo_d60

Figure 13: **Evaluation of resident mesenchymal niche activity for AT2 stem cells during fibrosis formation and resolution.**

a) 8-12 weeks-old female *Tg(Acta2-CreERT2)/+;tdTomato^{flox}* mice are used to lineage label *Acta2^{pos}* cells in saline at day14 and Bleo-Tam condition at day 14 and 60 post-bleo injury. **b)** Corresponding low and high magnification of IF staining against Rfp (tdTom^{pos}), Acta2 and DAPI, indicating the presence of tdTom^{pos} cells in the bronchiolar region as well as in the alveolar region in saline conditions at day14 and the presence of abundant tdTom^{pos} cells in the fibrotic region at day 14. Note the presence of tdTom^{pos} cells in the fibrotic region at day 60, which suggest that fibrosis is not completely resolved. **c)** Corresponding low and high magnification of H&E staining showing fibrosis formation at day 14 and the existence of fibrotic regions at day 60. **d)** Gating strategy to sort CD31/CD45/EpCam triple negative (rMC) positive for Sca1 (rMC Sca1^{Pos} cells) as well as AT2s (CD31/CD45 negative EpCam^{pos} Lysotracker^{pos}). AT2 Lyso^{pos} and rMC Sca1^{Pos} cells are co-cultured in Matrigel for 14 days (alveolosphere assay). **e)** Bright field pictures showing the formation of organoids when rMC Sca1^{pos} cells are isolated from Saline day 14 lungs and co-cultured with AT2s from non-injured C57BL/6 mice. Note that such mesenchymal niche activity is significantly reduced at the peak of fibrosis (Bleo day 14) and completely lost during fibrosis resolution (Bleo day 30 and day 60). **f)** Quantification of colony forming efficiency confirming the decrease in stem cell niche activity during fibrosis formation Bleo day 14 0.77% ± 0.09% (n=3) vs saline day 14 2.2% ± 0.20% (n=3) and the lack of recovery during fibrosis resolution Bleo day 30 0% ± 0% (n=3) and day 60 0% ± 0% (n=3). Scale bar: b: Low magnification-75µm, High magnification- 10µm; c: Low magnification- 500µm, High magnification- 50µm; and e: 200µm. Statistical analysis was performed using one-way ANOVA with Newman–Keuls post hoc test for multiple comparisons. *: $p<0.05$; **: $p<0.01$; ***: $p<0.001$

5. Discussion

5.1 Breaking the dogma of Acta2 positive cells in the lung.

Several lineage tracing studies using *Tg(Acta2-CreERT2)/+; tdTomato^{flox}* mice showed that *Acta2^{pos}* cells during embryonic and postnatal lung development contribute significantly to alveolar myofibroblasts; these cells are master regulators of secondary septa formation thereby increases alveolar space for gas exchange. However, *Acta2* expression is restricted only to ASMCs and VSMCs in the adult lung(El Agha, Moiseenko, et al., 2017; Moiseenko et al., 2017).

Interestingly, our scRNA-seq results are against the dogma that *Acta2^{pos}* cells contribute only to ASMCs and VSMCs; furthermore, in addition to them, we also identified various mesenchymal populations in the parenchymal region of the lung, including, alveolar fibroblasts, adventitial fibroblasts, peribronchial fibroblasts, pericytes, well as minor contributions to Cthrc1 fibroblasts (Figure 5a).

These surprising results might be due to the differential expression of Acta2 protein in the lung populations, Acta2 is highly expressed in the ASMCs and VSMCs (Figure 4c) and often ignores the low-expressing Acta2 cells in the parenchyma. Furthermore, different levels of tdTomato expressions are also observed in the lineage-labeled *Acta2^{pos}* cells. This shows the heterogeneity of the Acta2^{pos} population, as Rosa26 locus expression varies between different cell types.

In conclusion, we used scRNA-seq on sorted lineage-labeled *Acta2^{pos}* (tdTom^{pos}) cells, which contributed to multiple lineages and clustered them based on their anatomical locations (Figure 14) in homeostasis condition.

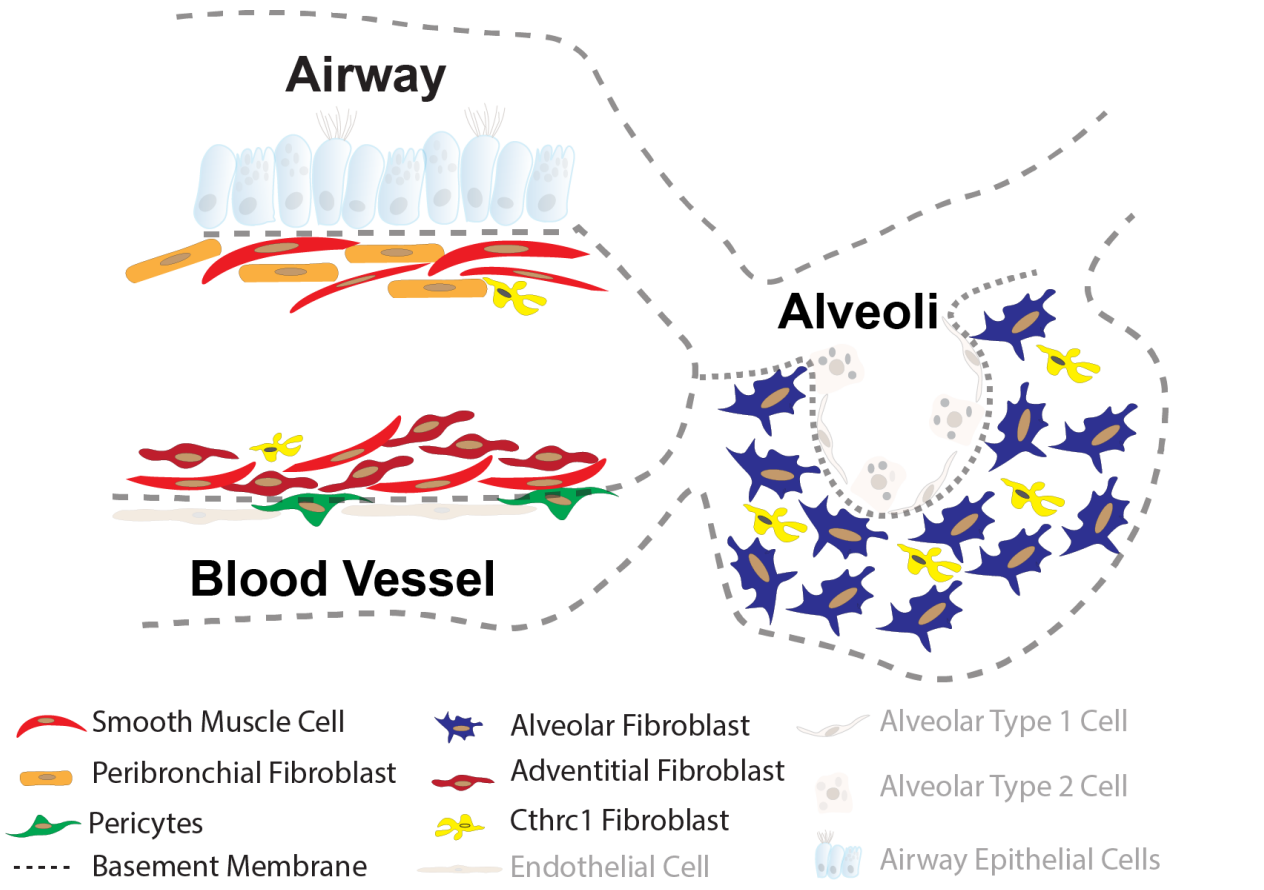

Figure 14: **Heterogeneity of *Acta2*^{pos} cells in the lung.**

Acta2^{pos} cells contribute to different mesenchymal hierarchies in the lung. Based on the anatomical location and expression signature they are categorized into alveolar fibroblasts which are located in the alveolar region, adventitial fibroblasts located around blood vessels, peribronchial fibroblasts around the bronchiolar region, airway and vascular smooth muscle cells, and a minor contribution to pericytes, and Cthrc1 fibroblasts.

5.2 Newly formed *Acta2*^{pos} cells during fibrosis massively contribute to the *Cthrc1*^{pos} aMYF lineage.

The hallmark of IPF is the deposition of excessive ECM and tissue scarring; this process is mediated and accelerated by aMYFs. It is widely believed that different sources contribute to aMYFs. Nevertheless, the contribution of lung rMCs to aMYF is still debated.

This study showed that pre-existing *Acta2*^{pos} minorly contributes to aMYF's during fibrosis formation. In contrast, cells acquire *Acta2* expression during fibrosis and massively contribute to aMYFs. Often researchers debate that in IPF, the entire lung mesenchyme gets activated and deposits excessive ECM (Peyser et al., 2019; Tsukui et al., 2020; Xie et al., 2018). Interestingly, our results show that the entire mesenchyme is responding/activated during fibrosis formation, but their contribution is negligible compared to the aMYF pool. However, we propose only three different mesenchymal populations, namely peribronchial, adventitial and alveolar fibroblasts that have potential to differentiate into aMYFs pool.

Surprisingly, a new population of alveolar fibroblasts arises, which were initially not identified in homeostatic conditions. We propose that this newly formed alveolar fibroblast cluster Al3 is initially *Acta2*^{neg} cells, but they acquire *Acta2*^{pos} status during fibrosis formation. The interesting fact with this Al3 cluster is that they express a high level of *Sfrp1,* which is proposed to be a Wnt signaling inhibitor. As aforementioned, Wnt is a potent fibrotic pathway that guides the differentiation of fibroblasts to aMYF (Cao et al., 2020). In addition, other studies also showed that Sfrp1 inhibited TGFβ in *vitro* cell cultures (De Langhe et al., 2014). This might be the reason that all the LIFs are not differentiating to aMYF's. The cells that lose Sfrp1 expression might be influenced by Wnt and TGFβ signaling, triggering the LIF to aMYF switch.

To sum up, during homeostatic conditions, *Acta2*^{pos} cells do not significantly contribute to aMYFs (Saline and Tam-Bleo conditions). *Acta2*^{pos} cells forming during fibrosis formation mainly arise from a pool of *Acta2*^{neg} cells that significantly contribute to aMYFs (Bleo-Tam condition) (Figure 15).

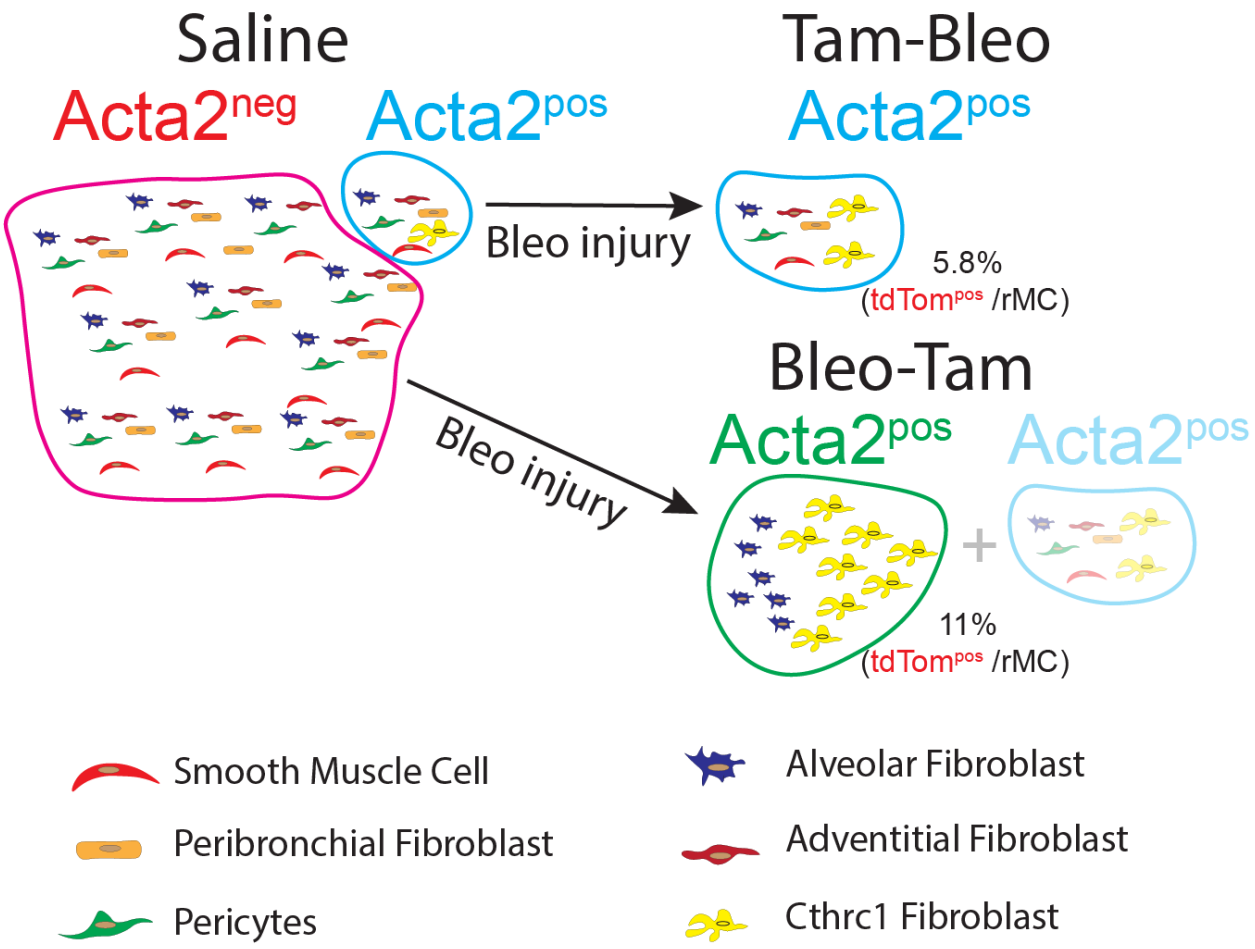

Figure15: ***De novo Acta2^{pos}* cells during fibrosis are massive contributors to fibrotic regions.**

Homeostatic *Acta2^{pos}* cells of different origins contribute minimally to aMYFs (Saline and Tam-Bleo conditions). In contrast, *de novo Acta2^{pos}* cells evolving during fibrosis are mostly arising from *Acta2^{neg}* cells of alveolar fibroblasts that significantly contribute to aMYFs (Bleo-Tam condition)

5.3 Heterogeneity of the *Cthrc1*^{pos} aMYF fibroblasts in IPF

It is widely proposed and accepted by the scientific community that aMYFs are a quite heterogeneous population (El Agha, Kramann, et al., 2017; Habiel & Hogaboam, 2017; Homps-Legrand, Crestani, & Mailleux, 2023; Hung, 2020). However, identifying and characterizing them was challenging due to the lack of specific signature markers and proper transgenic mice models.

Nevertheless, our study showed that the Cthrc1^{pos} aMYFs amplified in the context of fibrosis represent a heterogeneous population that was further classified into four different clusters (Ct1-4). Despite the clustering being based on *Cthrc1* expression, these 4 clusters displayed differentially expressed genes. The Ct1 cluster contains more of LIF's characteristics. Both Ct3 and Ct4 were observed only in the context of fibrosis formation, and they were cleared during fibrosis resolution. It is possible that Ct3 and Ct4 cells differentiated back to their native states, which remains to be defined or underwent apoptotic clearance.

Interestingly, Ct2 is the most abundant of all the clusters and shows the highest levels of *Cthrc1* expression. Furthermore, pathway analysis shows that cluster Ct2 is enriched with key fibrotic signaling pathways such as *Tgfβ* and *Wnt*, which suggests that LIF to aMYF differentiation is guided by Tgfβ and Wnt signaling.

In conclusion, Cthrc1^{pos} aMYFs are heterogeneous and arise from multiple sources. They respond differently during fibrosis resolution by either transitioning back to their native state or undergoing apoptotic clearance. Additionally, we found that CTHRC1^{pos} aMYF in human IPF data sets are heterogeneous (with some clusters enriched with LIF markers), thereby supporting this study.

5.4 LIF-AT2 stem cell niche is still hindered during fibrosis resolution

IPF is commonly diagnosed in older men and is unfortunately not curable and reversible (Garcia, 2011; Raghu et al., 2018). However, mice are capable of resolving fibrosis following bleomycin injury. This enabled scientists to understand key signaling regulators in fibrosis resolution which could be further translated into human IPF; however, studies

often use young mice. This is a limitation as IPF is a disease associated with aging. Therefore, instead of using young mice (2-3 months of age), it would be more appropriate to use elderly mice (12-18 months of age).

One of the hallmarks of fibrosis is the loss of the LIF-AT2 stem cell niche activity due to epithelial cell injury, dysregulated repair, alveolar regeneration, and impaired epithelial-LIF crosstalk. In mice models, the clearance of fibrotic lesions is considered fibrosis resolution. Nonetheless, regaining the lost AT2 cells and LIF-AT2 stem cell niche activity for restoring lung architecture and physiology is overlooked.

As aforementioned, the LIF-AT2 stem cell niche activity is lost with an increase of reactive oxygen species produced by Nox4 due to metabolic dysregulation, a hallmark of aging (Chanda et al., 2021). Various studies showed that NOX4 is elevated in IPF lungs and acts as a key regulator in fibroblast to myofibroblast transition. NOX4 increases ACTA2 and COL1a1 expression by activating SMAD2/3 phosphorylation. Interestingly, inhibition of NOX4 showed decreased ACTA2 and COL1a1 expression (Amara et al., 2010). Additionally, intraperitoneal administration of metformin attenuates lung fibrosis in mice by suppressing Nox4 (Sato et al., 2016).

A recent study demonstrated fibrotic CTHRC1^{pos} cells act as a pathological niche for human AT2 cells. This niche modulates and transdifferentiates AT2 into pathological basal cells (Kathiriya et al., 2022). These studies show that the loss of the homeostatic niche and the gain of the pathological niche are the key factors in the initiation and progression of IPF.

In conclusion, we also demonstrated, for the first time, that the resident mesenchymal cell activity, mainly carried out by the LIFs, does not recover during fibrosis resolution (Figure 13e and f). It further demonstrates that long-term damage to the vital LIF-AT2 interactions in this mouse model is still present despite the clearance of most of the fibrotic lesions. Furthermore, comparing the studies using aged mice around 12-18 months with young mice could be a different angle for advancing fibrosis research.

5.5 Evidence for a LIF-to-Cthrc1^{pos} aMYF reversible switch during fibrosis formation and resolution

In this study, we used lineage tracing of *Acta2*^{pos} cells in combination with FACS and scRNA-seq to investigate whether an alveolar fibroblast/lipofibroblast-to-Cthrc1^{pos}/activated myofibroblast reversible switch takes place during fibrosis formation and resolution in young mice following bleomycin administration. Figure 16 summarizes our results.

We propose that during fibrosis formation, the main contributors to *Cthrc1*^{pos} aMYF are *Acta2*^{neg} LIF^{high} alveolar fibroblasts, which following bleomycin administration, get activated and express a fibrotic signature and eventually differentiate into *Cthrc1*^{Low} LIF^{high} aMYF belonging to Ct1 cells. Ct1s further differentiate into Ct2 *Cthrc1*^{high} aMYF during fibrosis progression. During fibrosis resolution, the opposite occurs with Ct2 cells differentiating into Ct1 cells, eventually leading to *Cthrc1*^{neg} LIF^{high} Al2 alveolar fibroblasts. We also propose that Ct3 and Ct4 arise from peribronchial and adventitial fibroblast, respectively. As we could not detect Ct3 and Ct4 at d60 during resolution in our conditions, we could not determine their fate during resolution. Interestingly, examination of the *CTHRC1*^{pos} cells in human IPF lungs also indicated heterogeneity in this cluster, primarily made of myofibroblasts expressing a high level of the LIF marker *LIMCH1* supporting the connection between the MYF and LIF in the context of the human IPF.

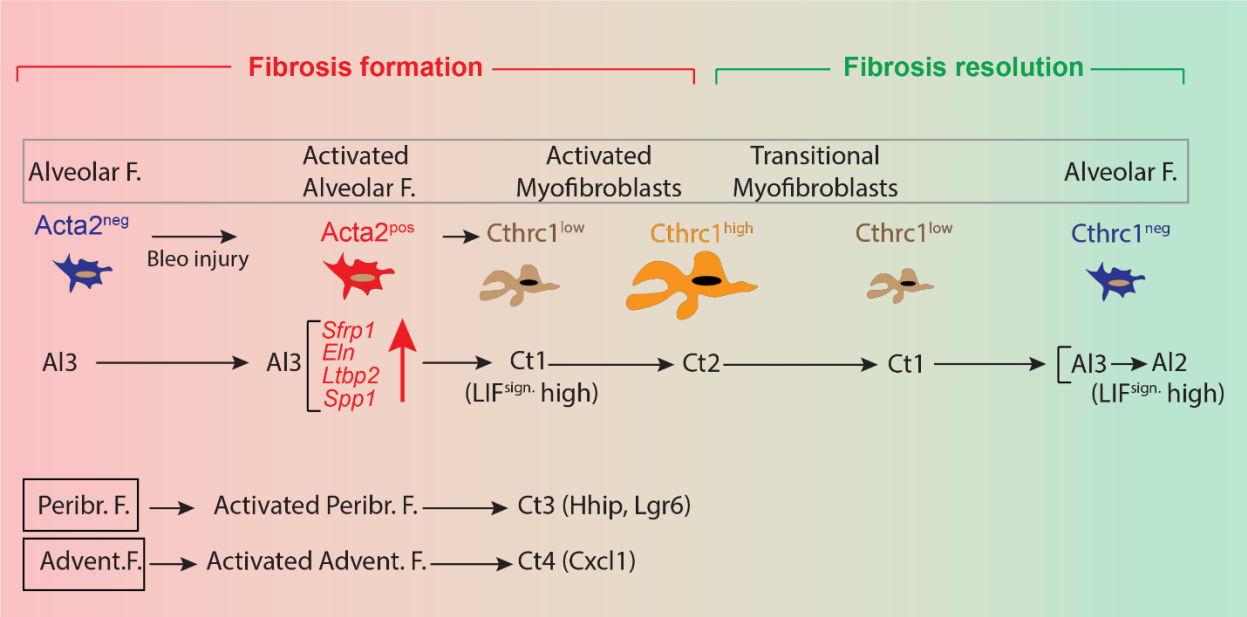

Figure 16: **Model of LIF-to-aMYF reversible switch during fibrosis formation and resolution**.

The main contributors during fibrosis formation to *Cthrc1*^{pos} aMYF (Ct1 and Ct2) are *Acta2*^{neg} LIF^{high} alveolar fibroblasts (Al3) which get activated and express a fibrotic signature and eventually differentiate into *Cthrc1*^{Low} LIF^{high} aMYF belonging to the Ct1 cluster. These Ct1 cells further differentiate into Ct2 *Cthrc1*^{high} aMYF. During fibrosis resolution, the opposite occurs with Ct2 cells differentiating into Ct1 cells, which will eventually give rise to *Cthrc1*^{neg} LIF^{high} alveolar fibroblasts (Al3 and Al2). We also propose that Ct3 and Ct4 arises from peribronchial and adventitial fibroblast respectively. As in our conditions, we could not detect Ct3 and Ct4 at d60 during resolution, we could not determine the fate.

5.6 LIF-to-aMYF reversible switch model for validating new drugs in IPF treatment

For surfactant synthesis, the LIF-AT2 interactions are essential. Parathyroid hormone-related protein (Pthrp), which is secreted by AT2 cells, interacts with the adjacent LIFs. Pparg is upregulated by Pthrp signaling, which increases Plin2 synthesis. For the production of surfactant, the transfer of neutral lipids from the lipofibroblast to AT2 requires Plin2 (V. K. Rehan & Torday, 2014).

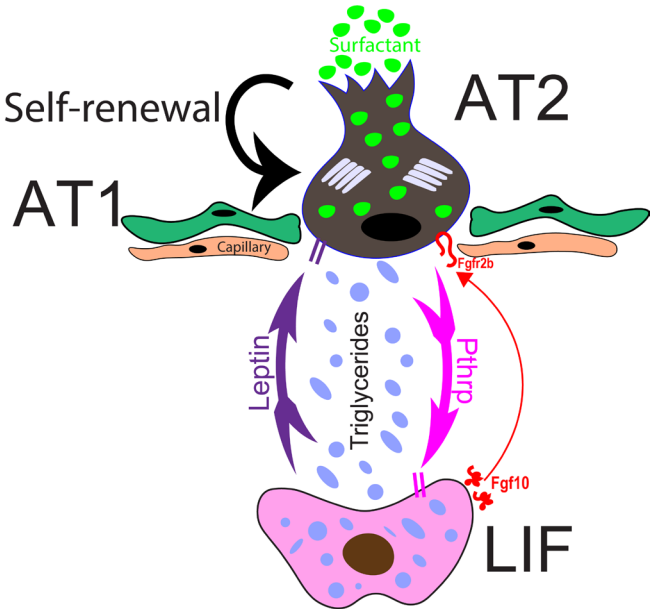

Figure 17: **LIF-AT2 crosstalk during homeostasis.**

Pthrp signaling is essential for surfactant synthesis and Fgf10-Fgfr2b signaling maintains AT2 cells survival in homeostatic conditions.

Interestingly, LIF to MYF transition was observed in neonatal rat lungs, with LIFs transdifferentiating into MYF in response to both hyperoxia and nicotine treatment (V. Rehan & Torday, 2003; V. K. Rehan et al., 2005). Furthermore, overexpressing Thy-1 and ciglitazone treatment led to an increase in Pparg and Plin2, with increased neutral lipid accumulation in fetal rat lung fibroblasts (Varisco, Ambalavanan, Whitsett, & Hagood, 2012). In a different study, the deletion of ALK5, a Tgfβ receptor element, in mesoderm

led to an increase in LIFs in the developing lung (Li et al., 2016). Additionally, pneumonectomy (PNX) mice with activated Pparg signaling by rosiglitazone displayed defective re-alveolarization due to an increase in LIF and decrease in myofibroblasts populations (Chen, Acciani, Le Cras, Lutzko, & Perl, 2012).

The TGFβ-mediated differentiation of pulmonary myofibroblasts and the synthesis of collagen were inhibited by PPARg activation by ciglitazone and rosiglitazone (Burgess et al., 2005). Additionally, our previous study had shown that metformin-induced activation of BMP2 signaling in aMYFs resulted in the upregulation of PLIN2 expression through PPARg activation and increased lipid droplet formation (Kheirollahi et al., 2019).

The reversible LIF to aMYF transition model will be vital for pre-clinical drug screening. For instance, creating new *in vitro* models with primary IPF lung fibroblast or WI-38 human embryonic lung fibroblast will be beneficial for testing and validating new drugs (Lingampally et al., 2020). Additionally, using known lipogenic inducible drugs such as metformin, rosiglitazone, and ciglitazone as a positive control to test the efficiency of new drugs will fast-track the development of new medications for IPF treatment.

5.7 Limitation of our scRNA-seq approach to study fibrosis formation and resolution.

Even though scRNA-seq is a powerful approach to identifying distinct cellular subpopulations within a given lineage, our approach would benefit in the future from gathering multiple time points during fibrosis formation and resolution. It is essential to integrate into future analyses the level of injury triggered by bleomycin. In our approach, we decided to settle for a mild level of fibrosis, which was nevertheless sufficient to trigger the formation of distinct clusters of *Cthrc1*^{pos} cells. The range of the pathways activated in these cells may depend on the level of injury.

Another limitation of our study is that we used only the *Tg(Acta2-CreERT2)* line to label the aMYFs. Interestingly, our results are against the dogma that *Acta2* is not a good marker for aMYF (Tsukui et al., 2020). While this may be true at the protein level, our *Tg(Acta2-CreERT2)* driver line successfully labeled the aMYF and, due to the non-leaky

nature of this line, allowed us to make the distinction between the *Acta2*^{pos} cells labeled before versus during injury. In the future, combining at least two different driver lines will be essential to enhance the labeling of the LIFs giving rise to the *Cthrc1*^{pos} aMYF. Such approaches may rely on the use of promoters for genes highly expressed in LIFs (such as *Fgf10*, *Tcf21*, *Scube2*) to drive Cre-ERT2 expression combined with the use of still to be generated *Cthrc1*$^{Dre\text{-}ERT2}$ mice.

Combining the Cre and Dre recombinases with the appropriate fluorescent reporter line will allow targeting only the *Cthrc1*^{pos} cells originating from the LIFs for single-cell transcriptomic analysis during fibrosis formation and resolution. Another important aspect will be to characterize further, using the same approach, the four different Cthrc1^{pos} subclusters identified in this study. In particular, it will be important to identify the critical cluster for the deleterious fibrosis phenotype.

6. Summary

Despite various studies and research, the initiation and progression of IPF are poorly understood. IPF is a fatal disease with no cure, and the median survival rate post diagnosis is 2-3 years. Currently, only two drugs, pirfenidone, and nintedanib have been used as the first-line therapy for IPF. However, they only slow the progression but do not cure the disease. Due to this, there is an urgent need to develop new therapeutic avenues (Y. M. Liu et al., 2017; Richeldi et al., 2014).

The initiation of IPF is believed to be caused by repetitive injury to the alveolar epithelium and recruitment of aMYFs. However, the cellular origin of aMYFs is still debated and controversial due to their heterogeneous origin and level of contribution to fibrotic regions during fibrosis. Furthermore, the fate of aMYFs and the underlying mechanisms that enhance fibrosis resolution are poorly understood and still unclear.

Considering that the aMYFs express *Acta2* and *Acta2*^{pos} cells significantly contribute to fibrotic regions, we used *Tg(Acta2-CreERT2); tdTomato*^{flox} mice to lineage-label aMYFs.

Firstly, our scRNA-seq results showed *Acta2*^{pos} cells contribute to different mesenchymal populations such as ASMCs, VSMCs, alveolar fibroblasts, adventitial fibroblasts, peribronchial fibroblasts, pericytes, and Cthrc1 fibroblasts. In the next step, we showed the pre-existing *Acta2*^{pos} cells displayed a minimal contribution to aMYFs during fibrosis formation. In contrast, newly formed *Acta2*^{pos} cells, during fibrosis formation, massively contribute to the aMYF pool. Furthermore, we showed these aMYFs are positive for Cthrc1.

Using fine clustering, we identified that the *Cthrc1*^{pos} aMYFs are a heterogeneous population, and we categorized them into four different clusters (Ct1-4). Interestingly, a different level of *Cthrc1* expression was observed within these four clusters. Furthermore, we have identified that the Ct1 cluster expresses high levels of the LIF signature and that the Ct2 cluster expresses a high level of *Cthrc1*. Moreover, data mining of human scRNA-seq from fibrotic lungs supported the presence of a heterogeneous *CTHRC1*^{pos} population.

Next, we have identified a new alveolar fibroblast population emerging during fibrosis formation (Bleo-Tam condition). These cells that originate from *Acta2*^{neg} alveolar fibroblasts and express high levels of fibrotic signature (*Sfrp1*, *Eln*, *Ltbp2*, *Spp1*^{high}) are suggested to differentiate into *Cthrc1*^{low} LIF^{high} Ct1 subcluster.

Finally, we provided evidence supporting a LIF-to-Cthrc1^{pos} aMYF reversible switch. We propose that the alveolar fibroblasts are activated during fibrosis formation, and *Acta2*^{neg} LIF^{high} alveolar fibroblasts differentiate to *Cthrc1*^{Low} LIF^{high} aMYFs (Ct1 cluster). With fibrosis progression, these cells further advance into *Cthrc1*^{high} aMYF (Ct2 cluster). During fibrosis resolution, the opposite occurs, *Cthrc1*^{high} aMYF Ct2 cluster differentiates into *Cthrc1*^{Low} LIF^{high} aMYFs Ct1 cluster, which eventually will differentiate back to alveolar fibroblasts.

In conclusion, in this study, we have demonstrated using a scRNA-seq approach that a LIF-to-aMYF reversible switch occurs during fibrosis formation and resolution. We have also further refined the heterogeneity of Cthrc1^{pos} aMYF populations, both in humans and mice, and proposed that they are of different origin. Furthermore, one subpopulation of Cthrc1^{pos} aMYFs, the Ct2 cluster, represents a potential translational target for fibrosis resolution.

7. Zusammenfassung

Trotz verschiedener Studien und Forschungen ist der Ausbruch und die Progression von IPF kaum verstanden. IPF ist eine tödliche Krankheit ohne Heilung und die mediane Überlebensrate nach der Diagnose beträgt 2-3 Jahre. Derzeit wurden nur zwei Medikamente, Pirfenidon und Nintedanib, als Erstlinientherapie von IPF eingesetzt. Sie verlangsamen jedoch nur das Fortschreiten, heilen aber nicht die Krankheit. Aufgrund dieser Tatsache besteht ein dringender Bedarf an der Entwicklung neuer therapeutischer Wege (Y. M. Liu et al., 2017; Richeldi et al., 2014).

Es wird angenommen, dass der Ausbruch von IPF durch wiederholte Verletzungen des Alveolarepithels und die Rekrutierung von aMYFs verursacht wird. Der zelluläre Ursprung von aMYFs wird aufgrund ihres heterogenen Ursprungs und ihres Beitrags zu fibrotischen Regionen während der Fibrose immer noch kontrovers diskutiert. Darüber hinaus ist das Schicksal von aMYFs und die zugrunde liegenden Mechanismen, die die Auflösung der Fibrose verbessern, schlecht verstanden und noch unklar.

In Anbetracht der Tatsache, dass die aMYFs *Acta2* exprimieren und dass Acta2^{pos} Zellen signifikant zu den fibrotischen Regionen beitragen, haben wir *Tg(Acta2-CreERT2);tdTomato^{flox}* Mäuse zum Herkunftsnachweis von aMYFs verwendet.

Erstens zeigten unsere scRNA-seq Ergebnisse, dass *Acta2^{pos}* Zellen zu verschiedenen mesenchymalen Populationen wie ASMCs, VSMCs, alveolären Fibroblasten, adventitiellen Fibroblasten, peribronchialen Fibroblasten, Perizyten und Cthrc1 Fibroblasten beitragen.

Im nächsten Schritt konnten wir zeigen, dass die bereits vorhandenen *Acta2^{pos}* Zellen während der Fibrosebildung einen minimalen Beitrag zur Bildung von aMYFs zeigten. Im Gegensatz dazu tragen neu gebildete *Acta2^{pos}* Zellen während der Fibrosebildung massiv zum aMYF Pool bei. Darüber hinaus haben wir gezeigt, dass diese aMYFs positiv für *Cthrc1* sind.

Durch fine clustering konnten wir feststellen, dass die *Cthrc1^{pos}* aMYFs eine heterogene Population sind, und wir haben sie in vier verschiedene Cluster (Ct1-4) kategorisiert.

Interessanterweise wurde innerhalb dieser vier Cluster ein unterschiedliches Niveau der *Cthrc1* Expression beobachtet. Wir haben festgestellt, dass der Ct1 Cluster ein hohes Niveau der LIF Signatur und der Ct2 Cluster einen hohen Grad an *Cthrc1* exprimiert. Darüber hinaus unterstützte Data Mining von humaner scRNA-seq aus fibrotischen Lungen das Vorhandensein einer heterogenen *CTHRC1*^{pos} Population.

Als nächstes haben wir eine neue alveoläre Fibroblastenpopulation identifiziert, die während der Fibrosebildung entsteht (Bleo-Tam-Kondition). Wir nehmen an, dass diese Zellen, die aus Acta2^{neg} alveolären Fibroblasten stammen und hohe fibrotische Signaturen (*Sfrp1, Eln, Ltbp2, Spp*1^{high}) aufweisen, in *Cthrc1*^{low} LIF^{high} Ct1 Subcluster differenzieren.

Schließlich lieferten wir Beweise für einen reversiblen LIF-zu-Cthrc1^{pos} aMYF-Schalter. Wir schließen daraus, dass während der Fibrosebildung die alveolären Fibroblasten aktiviert werden und *Acta2*^{neg} LIF^{high} alveoläre Fibroblasten zu *Cthrc1*^{Low} LIF^{high} aMYFs (Ct1-Cluster) differenzieren. Im Verlauf der Fibrose entwickeln sich diese Zellen weiter zu *Cthrc1*^{high} aMYF (Ct2-Cluster). Während der Auflösung der Fibrose tritt das Gegenteil auf, ein *Cthrc1*^{high} aMYF Cluster differenziert sich in einen *Cthrc1*^{Low} LIF^{high} aMYFs Ct1-Cluster, der sich schließlich wieder zu alveolären Fibroblasten zurück differenziert.

Zusammenfassend haben wir in dieser Studie mit einem scRNA-seq -Ansatz gezeigt, dass ein reversibler LIF-zu-aMYF -Wechsel während der Fibrosebildung und -auflösung stattfindet. Wir haben auch die Heterogenität von Cthrc1^{pos} aMYF-Populationen sowohl bei Menschen als auch bei Mäusen weiter definiert und schlagen vor, dass sie unterschiedlichen Ursprungs sind. Darüber hinaus stellt eine Subpopulation von Cthrc1^{pos} aMYFs, das Ct2-Cluster, ein potenzielles Translationsziel für die Auflösung von Fibrosen dar.

8. References

Adams, T. S., Schupp, J. C., Poli, S., Ayaub, E. A., Neumark, N., Ahangari, F., . . . Kaminski, N. (2020). Single-cell RNA-seq reveals ectopic and aberrant lung-resident cell populations in idiopathic pulmonary fibrosis. *Sci Adv, 6*(28), eaba1983. doi:10.1126/sciadv.aba1983

Ahmadvand, N., Khosravi, F., Lingampally, A., Wasnick, R., Vazquez-Armendariz, A. I., Carraro, G., . . . Bellusci, S. (2021). Identification of a novel subset of alveolar type 2 cells enriched in PD-L1 and expanded following pneumonectomy. *Eur Respir J, 58*(5). doi:10.1183/13993003.04168-2020

Al Alam, D., El Agha, E., Sakurai, R., Kheirollahi, V., Moiseenko, A., Danopoulos, S., . . . Bellusci, S. (2015). Evidence for the involvement of fibroblast growth factor 10 in lipofibroblast formation during embryonic lung development. *Development, 142*(23), 4139-4150. doi:10.1242/dev.109173

Amara, N., Goven, D., Prost, F., Muloway, R., Crestani, B., & Boczkowski, J. (2010). NOX4/NADPH oxidase expression is increased in pulmonary fibroblasts from patients with idiopathic pulmonary fibrosis and mediates TGFbeta1-induced fibroblast differentiation into myofibroblasts. *Thorax, 65*(8), 733-738. doi:10.1136/thx.2009.113456

Ashcroft, T., Simpson, J. M., & Timbrell, V. (1988). Simple method of estimating severity of pulmonary fibrosis on a numerical scale. *J Clin Pathol, 41*(4), 467-470. doi:10.1136/jcp.41.4.467

Barkauskas, C. E., Cronce, M. J., Rackley, C. R., Bowie, E. J., Keene, D. R., Stripp, B. R., . . . Hogan, B. L. M. (2013). Type 2 alveolar cells are stem cells in adult lung. *Journal of Clinical Investigation, 123*(7), 3025-3036. doi:10.1172/Jci68782

Binks, A. P., Beyer, M., Miller, R., & LeClair, R. J. (2017). Cthrc1 lowers pulmonary collagen associated with bleomycin-induced fibrosis and protects lung function. *Physiol Rep, 5*(5). doi:10.14814/phy2.13115

Brownfield, D. G., de Arce, A. D., Ghelfi, E., Gillich, A., Desai, T. J., & Krasnow, M. A. (2022). Alveolar cell fate selection and lifelong maintenance of AT2 cells by FGF signaling. *Nat Commun, 13*(1), 7137. doi:doi.org/10.1038/s41467-022-34059-1

Bueno, M., Calyeca, J., Rojas, M., & Mora, A. L. (2020). Mitochondria dysfunction and metabolic reprogramming as drivers of idiopathic pulmonary fibrosis. *Redox Biol, 33*, 101509. doi:10.1016/j.redox.2020.101509

Burgess, H. A., Daugherty, L. E., Thatcher, T. H., Lakatos, H. F., Ray, D. M., Redonnet, M., . . . Sime, P. J. (2005). PPARgamma agonists inhibit TGF-beta induced pulmonary myofibroblast differentiation and collagen production: implications for therapy of lung fibrosis. *Am J Physiol Lung Cell Mol Physiol, 288*(6), L1146-1153. doi:10.1152/ajplung.00383.2004

Cao, H., Chen, X., Hou, J., Wang, C., Xiang, Z., Shen, Y., & Han, X. (2020). The Shh/Gli signaling cascade regulates myofibroblastic activation of lung-resident mesenchymal stem cells via the modulation of Wnt10a expression during pulmonary fibrogenesis. *Lab Invest, 100*(3), 363-377. doi:10.1038/s41374-019-0316-8

Chanda, D., Rehan, M., Smith, S. R., Dsouza, K. G., Wang, Y., Bernard, K., . . . Thannickal, V. J. (2021). Mesenchymal stromal cell aging impairs the self-organizing capacity of lung alveolar epithelial stem cells. *Elife, 10*. doi:10.7554/eLife.68049

Chen, L., Acciani, T., Le Cras, T., Lutzko, C., & Perl, A. K. (2012). Dynamic regulation of platelet-derived growth factor receptor alpha expression in alveolar fibroblasts during realveolarization. *Am J Respir Cell Mol Biol, 47*(4), 517-527. doi:10.1165/rcmb.2012-0030OC

De Langhe, E., Aznar-Lopez, C., De Vooght, V., Vanoirbeek, J. A., Luyten, F. P., & Lories, R. J. (2014). Secreted frizzled related proteins inhibit fibrosis in vitro but appear redundant in vivo. *Fibrogenesis Tissue Repair, 7*, 14. doi:10.1186/1755-1536-7-14

El Agha, E., Herold, S., Al Alam, D., Quantius, J., MacKenzie, B., Carraro, G., . . . Bellusci, S. (2014). Fgf10-positive cells represent a progenitor cell population during lung development and postnatally. *Development, 141*(2), 296-306. doi:10.1242/dev.099747

El Agha, E., Kramann, R., Schneider, R. K., Li, X., Seeger, W., Humphreys, B. D., & Bellusci, S. (2017). Mesenchymal Stem Cells in Fibrotic Disease. *Cell Stem Cell, 21*(2), 166-177. doi:10.1016/j.stem.2017.07.011

El Agha, E., Moiseenko, A., Kheirollahi, V., De Langhe, S., Crnkovic, S., Kwapiszewska, G., . . . Bellusci, S. (2017). Two-Way Conversion between Lipogenic and Myogenic Fibroblastic Phenotypes Marks the Progression and Resolution of Lung Fibrosis. *Cell Stem Cell, 20*(2), 261-273 e263. doi:10.1016/j.stem.2016.10.004

Fernandez, I. E., & Eickelberg, O. (2012). The impact of TGF-beta on lung fibrosis: from targeting to biomarkers. *Proc Am Thorac Soc, 9*(3), 111-116. doi:10.1513/pats.201203-023AW

Gabbiani, G., Ryan, G. B., & Majne, G. (1971). Presence of modified fibroblasts in granulation tissue and their possible role in wound contraction. *Experientia, 27*(5), 549-550. doi:10.1007/BF02147594

Garcia, C. K. (2011). Idiopathic pulmonary fibrosis: update on genetic discoveries. *Proc Am Thorac Soc, 8*(2), 158-162. doi:10.1513/pats.201008-056MS

Habermann, A. C., Gutierrez, A. J., Bui, L. T., Yahn, S. L., Winters, N. I., Calvi, C. L., . . . Kropski, J. A. (2020). Single-cell RNA sequencing reveals profibrotic roles of distinct epithelial and mesenchymal lineages in pulmonary fibrosis. *Sci Adv, 6*(28), eaba1972. doi:DOI: 10.1126/sciadv.aba1972

Habiel, D. M., & Hogaboam, C. M. (2017). Heterogeneity of Fibroblasts and Myofibroblasts in Pulmonary Fibrosis. *Curr Pathobiol Rep, 5*(2), 101-110. doi:10.1007/s40139-017-0134-x

Hao, Y., Hao, S., Andersen-Nissen, E., Mauck, W. M., 3rd, Zheng, S., Butler, A., . . . Satija, R. (2021). Integrated analysis of multimodal single-cell data. *Cell, 184*(13), 3573-3587 e3529. doi:10.1016/j.cell.2021.04.048

Henderson, W. R., Jr., Chi, E. Y., Ye, X., Nguyen, C., Tien, Y. T., Zhou, B., . . . Kahn, M. (2010). Inhibition of Wnt/beta-catenin/CREB binding protein (CBP) signaling reverses pulmonary fibrosis. *Proc Natl Acad Sci U S A, 107*(32), 14309-14314. doi:10.1073/pnas.1001520107

Homps-Legrand, M., Crestani, B., & Mailleux, A. A. (2023). Origins of pathological myofibroblasts in lung fibrosis: insights from lineage tracing mouse models in the single-cell RNA sequencing era. *Am J Physiol Lung Cell Mol Physiol, 324*(6), L737-L746. doi:10.1152/ajplung.00229.2022

Hung, C. F. (2020). Origin of Myofibroblasts in Lung Fibrosis. *Current Tissue Microenvironment Reports, 1*(4), 155-162. doi:10.1007/s43152-020-00022-9

Jin, J., Togo, S., Kadoya, K., Tulafu, M., Namba, Y., Iwai, M., . . . Takahashi, K. (2019). Pirfenidone attenuates lung fibrotic fibroblast responses to transforming growth factor-beta1. *Respir Res, 20*(1), 119. doi:10.1186/s12931-019-1093-z

Jones, M. R., Dilai, S., Lingampally, A., Chao, C. M., Danopoulos, S., Carraro, G., . . . Bellusci, S. (2018). A Comprehensive Analysis of Fibroblast Growth Factor Receptor 2b Signaling on Epithelial Tip Progenitor Cells During Early Mouse Lung Branching Morphogenesis. *Front Genet, 9*, 746. doi:10.3389/fgene.2018.00746

Jones, M. R., Lingampally, A., Dilai, S., Shrestha, A., Stripp, B., Helmbacher, F., . . . Bellusci, S. (2019). Characterization of Tg(Etv4-GFP) and Etv5 (RFP) Reporter Lines in the Context of Fibroblast Growth Factor 10 Signaling During Mouse Embryonic Lung Development. *Front Genet, 10*, 178. doi:10.3389/fgene.2019.00178

Jones, M. R., Lingampally, A., Wu, J., Sedighi, J., Ahmadvand, N., Wilhelm, J., . . . Chao, C. M. (2020). Evidence for Overlapping and Distinct Biological Activities and Transcriptional Targets Triggered by Fibroblast Growth Factor Receptor 2b Signaling between Mid- and Early Pseudoglandular Stages of Mouse Lung Development. *Cells, 9*(5). doi:10.3390/cells9051274

Kathiriya, J. J., Wang, C., Zhou, M., Brumwell, A., Cassandras, M., Le Saux, C. J., . . . Peng, T. (2022). Human alveolar type 2 epithelium transdifferentiates into metaplastic KRT5(+) basal cells. *Nat Cell Biol, 24*(1), 10-23. doi:10.1038/s41556-021-00809-4

Kheirollahi, V., Wasnick, R. M., Biasin, V., Vazquez-Armendariz, A. I., Chu, X., Moiseenko, A., . . . El Agha, E. (2019). Metformin induces lipogenic differentiation

in myofibroblasts to reverse lung fibrosis. *Nat Commun, 10*(1), 2987. doi:10.1038/s41467-019-10839-0

Kim, K. K., Kugler, M. C., Wolters, P. J., Robillard, L., Galvez, M. G., Brumwell, A. N., . . . Chapman, H. A. (2006). Alveolar epithelial cell mesenchymal transition develops in vivo during pulmonary fibrosis and is regulated by the extracellular matrix. *Proc Natl Acad Sci U S A, 103*(35), 13180-13185. doi:10.1073/pnas.0605669103

LeClair, R., & Lindner, V. (2007). The role of collagen triple helix repeat containing 1 in injured arteries, collagen expression, and transforming growth factor beta signaling. *Trends Cardiovasc Med, 17*(6), 202-205. doi:10.1016/j.tcm.2007.05.004

Lee, J. H., Tammela, T., Hofree, M., Choi, J., Marjanovic, N. D., Han, S., . . . Kim, C. F. (2017). Anatomically and Functionally Distinct Lung Mesenchymal Populations Marked by Lgr5 and Lgr6. *Cell, 170*(6), 1149-1163 e1112. doi:10.1016/j.cell.2017.07.028

Li, A., Ma, S., Smith, S. M., Lee, M. K., Fischer, A., Borok, Z., . . . Minoo, P. (2016). Mesodermal ALK5 controls lung myofibroblast versus lipofibroblast cell fate. *BMC Biol, 14*, 19. doi:10.1186/s12915-016-0242-9

Liberti, D. C., Kremp, M. M., Liberti, W. A., 3rd, Penkala, I. J., Li, S., Zhou, S., & Morrisey, E. E. (2021). Alveolar epithelial cell fate is maintained in a spatially restricted manner to promote lung regeneration after acute injury. *Cell Rep, 35*(6), 109092. doi:10.1016/j.celrep.2021.109092

Lingampally, A., Jones, M. R., Bagari, S., Chen, C., Rivetti, S., & Bellusci, S. (2020). Use of the Reversible Myogenic to Lipogenic Transdifferentiation Switch for the Design of Pre-clinical Drug Screening in Idiopathic Pulmonary Fibrosis. *Front Bioeng Biotechnol, 8*, 569865. doi:10.3389/fbioe.2020.569865

Liu, X., Rowan, S. C., Liang, J., Yao, C., Huang, G., Deng, N., . . . Jiang, D. (2021). Categorization of lung mesenchymal cells in development and fibrosis. *iScience, 24*(6), 102551. doi:10.1016/j.isci.2021.102551

Liu, Y. M., Nepali, K., & Liou, J. P. (2017). Idiopathic Pulmonary Fibrosis: Current Status, Recent Progress, and Emerging Targets. *J Med Chem, 60*(2), 527-553. doi:10.1021/acs.jmedchem.6b00935

Marriott, S., Baskir, R. S., Gaskill, C., Menon, S., Carrier, E. J., Williams, J., . . . Majka, S. M. (2014). ABCG2pos lung mesenchymal stem cells are a novel pericyte subpopulation that contributes to fibrotic remodeling. *Am J Physiol Cell Physiol, 307*(8), C684-698. doi:10.1152/ajpcell.00114.2014

McQualter, J. L., McCarty, R. C., Van der Velden, J., O'Donoghue, R. J., Asselin-Labat, M. L., Bozinovski, S., & Bertoncello, I. (2013). TGF-beta signaling in stromal cells acts upstream of FGF-10 to regulate epithelial stem cell growth in the adult lung. *Stem Cell Res, 11*(3), 1222-1233. doi:10.1016/j.scr.2013.08.007

Mei, D., Zhu, Y., Zhang, L., & Wei, W. (2020). The Role of CTHRC1 in Regulation of Multiple Signaling and Tumor Progression and Metastasis. *Mediators Inflamm, 2020*, 9578701. doi:10.1155/2020/9578701

Moiseenko, A., Kheirollahi, V., Chao, C. M., Ahmadvand, N., Quantius, J., Wilhelm, J., . . . Bellusci, S. (2017). Origin and characterization of alpha smooth muscle actin-positive cells during murine lung development. *Stem Cells, 35*(6), 1566-1578. doi:10.1002/stem.2615

Mora, A. L., Rojas, M., Pardo, A., & Selman, M. (2017). Emerging therapies for idiopathic pulmonary fibrosis, a progressive age-related disease. *Nat Rev Drug Discov, 16*(11), 755-772. doi:10.1038/nrd.2017.170

Myngbay, A., Manarbek, L., Ludbrook, S., & Kunz, J. (2021). The Role of Collagen Triple Helix Repeat-Containing 1 Protein (CTHRC1) in Rheumatoid Arthritis. *Int J Mol Sci, 22*(5). doi:10.3390/ijms22052426

O'Hare, K. H., & Sheridan, M. N. (1970). Electron microscopic observations on the morphogenesis of the albino rat lung, with special reference to pulmonary epithelial cells. *Am J Anat, 127*(2), 181-205. doi:10.1002/aja.1001270205

Parimon, T., Yao, C., Stripp, B. R., Noble, P. W., & Chen, P. (2020). Alveolar Epithelial Type II Cells as Drivers of Lung Fibrosis in Idiopathic Pulmonary Fibrosis. *Int J Mol Sci, 21*(7). doi:10.3390/ijms21072269

Park, E. H., Kim, S., Jo, J. Y., Kim, S. J., Hwang, Y., Kim, J. M., . . . Koh, S. S. (2013). Collagen triple helix repeat containing-1 promotes pancreatic cancer progression by regulating migration and adhesion of tumor cells. *Carcinogenesis, 34*(3), 694-702. doi:10.1093/carcin/bgs378

Park, J., Ivey, M. J., Deana, Y., Riggsbee, K. L., Sorensen, E., Schwabl, V., . . . Tallquist, M. D. (2019). The Tcf21 lineage constitutes the lung lipofibroblast population. *Am J Physiol Lung Cell Mol Physiol, 316*(5), L872-L885. doi:10.1152/ajplung.00254.2018

Peyser, R., MacDonnell, S., Gao, Y., Cheng, L., Kim, Y., Kaplan, T., . . . Morton, L. (2019). Defining the Activated Fibroblast Population in Lung Fibrosis Using Single-Cell Sequencing. *Am J Respir Cell Mol Biol, 61*(1), 74-85. doi:10.1165/rcmb.2018-0313OC

Phan, S. H. (2012). Genesis of the myofibroblast in lung injury and fibrosis. *Proc Am Thorac Soc, 9*(3), 148-152. doi:10.1513/pats.201201-011AW

Phillips, R. J., Burdick, M. D., Hong, K., Lutz, M. A., Murray, L. A., Xue, Y. Y., . . . Strieter, R. M. (2004). Circulating fibrocytes traffic to the lungs in response to CXCL12 and mediate fibrosis. *J Clin Invest, 114*(3), 438-446. doi:10.1172/JCI20997

Piersma, B., Bank, R. A., & Boersema, M. (2015). Signaling in Fibrosis: TGF-beta, WNT, and YAP/TAZ Converge. *Front Med (Lausanne), 2*, 59. doi:10.3389/fmed.2015.00059

Plantier, L., Cazes, A., Dinh-Xuan, A. T., Bancal, C., Marchand-Adam, S., & Crestani, B. (2018). Physiology of the lung in idiopathic pulmonary fibrosis. *Eur Respir Rev, 27*(147). doi:10.1183/16000617.0062-2017

Pyagay, P., Heroult, M., Wang, Q., Lehnert, W., Belden, J., Liaw, L., . . . Lindner, V. (2005). Collagen triple helix repeat containing 1, a novel secreted protein in injured and diseased arteries, inhibits collagen expression and promotes cell migration. *Circ Res, 96*(2), 261-268. doi:10.1161/01.RES.0000154262.07264.12

Raghu, G., Remy-Jardin, M., Myers, J. L., Richeldi, L., Ryerson, C. J., Lederer, D. J., . . . Latin American Thoracic, S. (2018). Diagnosis of Idiopathic Pulmonary Fibrosis. An Official ATS/ERS/JRS/ALAT Clinical Practice Guideline. *Am J Respir Crit Care Med, 198*(5), e44-e68. doi:10.1164/rccm.201807-1255ST

Redente, E. F., Jacobsen, K. M., Solomon, J. J., Lara, A. R., Faubel, S., Keith, R. C., . . . Riches, D. W. (2011). Age and sex dimorphisms contribute to the severity of bleomycin-induced lung injury and fibrosis. *Am J Physiol Lung Cell Mol Physiol, 301*(4), L510-518. doi:10.1152/ajplung.00122.2011

Rehan, V., & Torday, J. (2003). Hyperoxia augments pulmonary lipofibroblast-to-myofibroblast transdifferentiation. *Cell Biochem Biophys, 38*(3), 239-250. doi:10.1385/cbb:38:3:239

Rehan, V. K., & Torday, J. S. (2014). The lung alveolar lipofibroblast: an evolutionary strategy against neonatal hyperoxic lung injury. *Antioxid Redox Signal, 21*(13), 1893-1904. doi:10.1089/ars.2013.5793

Rehan, V. K., Wang, Y., Sugano, S., Romero, S., Chen, X., Santos, J., . . . Torday, J. S. (2005). Mechanism of nicotine-induced pulmonary fibroblast transdifferentiation. *Am J Physiol Lung Cell Mol Physiol, 289*(4), L667-676. doi:10.1152/ajplung.00358.2004

Richeldi, L., du Bois, R. M., Raghu, G., Azuma, A., Brown, K. K., Costabel, U., . . . Investigators, I. T. (2014). Efficacy and safety of nintedanib in idiopathic pulmonary fibrosis. *N Engl J Med, 370*(22), 2071-2082. doi:10.1056/NEJMoa1402584

Rock, J. R., Barkauskas, C. E., Cronce, M. J., Xue, Y., Harris, J. R., Liang, J., . . . Hogan, B. L. (2011). Multiple stromal populations contribute to pulmonary fibrosis without evidence for epithelial to mesenchymal transition. *Proc Natl Acad Sci U S A, 108*(52), E1475-1483. doi:10.1073/pnas.1117988108

Sato, N., Takasaka, N., Yoshida, M., Tsubouchi, K., Minagawa, S., Araya, J., . . . Kuwano, K. (2016). Metformin attenuates lung fibrosis development via NOX4 suppression. *Respir Res, 17*(1), 107. doi:10.1186/s12931-016-0420-x

Schipke, J., Kuhlmann, S., Hegermann, J., Fassbender, S., Kuhnel, M., Jonigk, D., & Muhlfeld, C. (2021). Lipofibroblasts in Structurally Normal, Fibrotic, and Emphysematous Human Lungs. *Am J Respir Crit Care Med, 204*(2), 227-230. doi:10.1164/rccm.202101-0043LE

Selman, M., & Pardo, A. (2006). Role of epithelial cells in idiopathic pulmonary fibrosis: from innocent targets to serial killers. *Proc Am Thorac Soc, 3*(4), 364-372. doi:10.1513/pats.200601-003TK

Sgalla, G., Biffi, A., & Richeldi, L. (2016). Idiopathic pulmonary fibrosis: Diagnosis, epidemiology and natural history. *Respirology, 21*(3), 427-437. doi:10.1111/resp.12683

Sgalla, G., Iovene, B., Calvello, M., Ori, M., Varone, F., & Richeldi, L. (2018). Idiopathic pulmonary fibrosis: pathogenesis and management. *Respir Res, 19*(1), 32. doi:10.1186/s12931-018-0730-2

Taghizadeh, S., Chao, C. M., Guenther, S., Glaser, L., Gersmann, L., Michel, G., . . . Rivetti, S. (2022). FGF10 Triggers De Novo Alveologenesis in a Bronchopulmonary Dysplasia Model: Impact on Resident Mesenchymal Niche Cells. *Stem Cells, 40*(6), 605-617. doi:10.1093/stmcls/sxac025

Taghizadeh, S., Heiner, M., Vazquez-Armendariz, A. I., Wilhelm, J., Herold, S., Chen, C., . . . Bellusci, S. (2021). Characterization in mice of the resident mesenchymal niche maintaining AT2 stem cell proliferation in homeostasis and disease. *Stem Cells, 39*(10), 1382-1394. doi:10.1002/stem.3423

Tahedl, D., Wirkes, A., Tschanz, S. A., Ochs, M., & Muhlfeld, C. (2014). How common is the lipid body-containing interstitial cell in the mammalian lung? *Am J Physiol Lung Cell Mol Physiol, 307*(5), L386-394. doi:10.1152/ajplung.00131.2014

Tashiro, J., Rubio, G. A., Limper, A. H., Williams, K., Elliot, S. J., Ninou, I., . . . Glassberg, M. K. (2017). Exploring Animal Models That Resemble Idiopathic Pulmonary Fibrosis. *Front Med (Lausanne), 4*, 118. doi:10.3389/fmed.2017.00118

Travaglini, K. J., Nabhan, A. N., Penland, L., Sinha, R., Gillich, A., Sit, R. V., . . . Krasnow, M. A. (2020). A molecular cell atlas of the human lung from single-cell RNA sequencing. *Nature, 587*(7835), 619-625. doi:10.1038/s41586-020-2922-4

Tsukui, T., Sun, K. H., Wetter, J. B., Wilson-Kanamori, J. R., Hazelwood, L. A., Henderson, N. C., . . . Sheppard, D. (2020). Collagen-producing lung cell atlas identifies multiple subsets with distinct localization and relevance to fibrosis. *Nat Commun, 11*(1), 1920. doi:10.1038/s41467-020-15647-5

Vaccaro, C., & Brody, J. S. (1978). Ultrastructure of developing alveoli. I. The role of the interstitial fibroblast. *Anat Rec, 192*(4), 467-479. doi:10.1002/ar.1091920402

Varisco, B. M., Ambalavanan, N., Whitsett, J. A., & Hagood, J. S. (2012). Thy-1 signals through PPARgamma to promote lipofibroblast differentiation in the developing lung. *Am J Respir Cell Mol Biol, 46*(6), 765-772. doi:10.1165/rcmb.2011-0316OC

Welch, J. D., Kozareva, V., Ferreira, A., Vanderburg, C., Martin, C., & Macosko, E. Z. (2019). Single-Cell Multi-omic Integration Compares and Contrasts Features of Brain Cell Identity. *Cell, 177*(7), 1873-1887 e1817. doi:10.1016/j.cell.2019.05.006

Wipff, P. J., Rifkin, D. B., Meister, J. J., & Hinz, B. (2007). Myofibroblast contraction activates latent TGF-beta1 from the extracellular matrix. *J Cell Biol, 179*(6), 1311-1323. doi:10.1083/jcb.200704042

Wu, H., Yu, Y., Huang, H., Hu, Y., Fu, S., Wang, Z., . . . Tang, N. (2020). Progressive Pulmonary Fibrosis Is Caused by Elevated Mechanical Tension on Alveolar Stem Cells. *Cell, 180*(1), 107-121 e117. doi:10.1016/j.cell.2019.11.027

Xie, T., Wang, Y., Deng, N., Huang, G., Taghavifar, F., Geng, Y., . . . Jiang, D. (2018). Single-Cell Deconvolution of Fibroblast Heterogeneity in Mouse Pulmonary Fibrosis. *Cell Rep, 22*(13), 3625-3640. doi:10.1016/j.celrep.2018.03.010

Yao, C., Guan, X., Carraro, G., Parimon, T., Liu, X., Huang, G., . . . Stripp, B. R. (2021). Senescence of Alveolar Type 2 Cells Drives Progressive Pulmonary Fibrosis. *Am J Respir Crit Care Med, 203*(6), 707-717. doi:10.1164/rccm.202004-1274OC

Zepp, J. A., Zacharias, W. J., Frank, D. B., Cavanaugh, C. A., Zhou, S., Morley, M. P., & Morrisey, E. E. (2017). Distinct Mesenchymal Lineages and Niches Promote Epithelial Self-Renewal and Myofibrogenesis in the Lung. *Cell, 170*(6), 1134-1148 e1110. doi:10.1016/j.cell.2017.07.034

Zhao, X., Kwan, J. Y. Y., Yip, K., Liu, P. P., & Liu, F. F. (2020). Targeting metabolic dysregulation for fibrosis therapy. *Nat Rev Drug Discov, 19*(1), 57-75. doi:10.1038/s41573-019-0040-5

9. Acknowledgements

First and foremost, I would like to express my sincere gratitude to my professor, Saverio Bellusci, for giving me the opportunity to join Bellusci Lab. His guidance and constructive criticism during my master's and doctoral studies is phenomenal and irreplaceable, I am grateful for that.

I would also express my special gratitude to Prof. Elie El Agha, Prof. Christoph Rummel, Prof. Bernard Mari, Marin Truchi, Prof. Helen Makarenkova, and Dr. Olivier Mauduit for their help and valuable feedback during my thesis.

I would like to express my special thanks to Kerstin, Esme, Mahsa, Xuran, and all Bellusci lab colleagues for their help with various aspects of the lab and scientific discussions.

I express my hearty thanks to Dr. Nabham Rai, Dr. Stefan Hadzic, Dr. Ana Ivonne Vazquez-Armendariz, Dr. Stefan Günther, Dr. Janine Koepke, Dr. Martina Korfei, Dr. Ingrid Henneke, and Dr. Thomas Sonntag. Without your support and help, the consistency in my work would be hard to imagine.

I am pleased to thank Heike, Cho (Prof. Cho Ming Chao), and Evelyn Pomar Bellusci for their help and support during my difficult times.

I thank my friends Santosh, Hemant, Vamshi, Srikanth, Tamriko, Imran, Shrinath, Sumit, Tejaswini, Kavya, Kripa, Sagar, Kalyan, Rahul, and Aravinth for their friendship and helping nature.

I am forever grateful to my parents, Manjula and Sammireddy, for their unconditional love and support. In addition, I thank my sister Pranitha, my brother-in-law Anil, and my niece Shanvika for their endless love and support. Finally, I would like to thank my best half and the pillar of my life, Shirisha, for always being there for me, with patience, throughout this journey and never complaining, even in the challenging times of her life. I would not have achieved anything in my life without the support of my family.

Finally, to my daughter Anika, I will love you forever, and kisses from dada.